Enhancing the conductivity of bacterial cellulose/polyvinyl alcohol composite for the development of flexible transparent electrodes

By

Modisa Maatseke Ntobeng

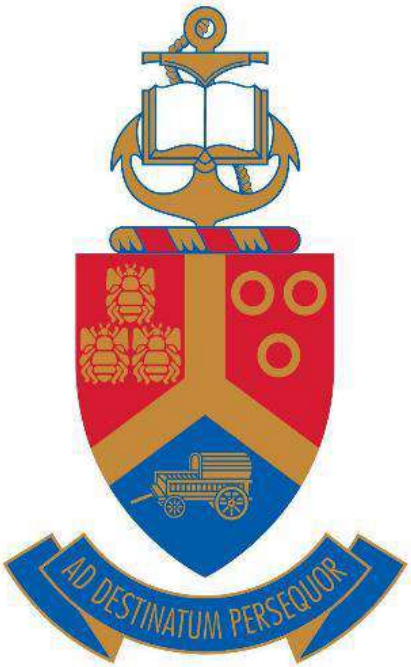

Submitted in partial fulfilment of the requirements for the degree

Magister Scientiae

In the Faculty of Natural and Agricultural Science

Department of Physics

Supervisor: Prof. M. M. Diale

Co-supervisor: Prof. N. Nombona

November 2024

Declaration 1

I, Modisa Maatseke Ntobeng, declare that the dissertation, which I hereby submit for the degree Magister Scientiae (MSc) in the Department of Physics at the University of Pretoria is my work and has not been submitted previously by me for a degree at this or any other institution.

Declaration 2 - Publications

Chapter 3

Optimisation of the hole transport layer in polymer solar cell MM Ntobeng, TE Seimela and M Diale. DOI: The 67th Annual Conference of the South African Institute of Physics (SAIP) manuscript page 196-201

In preparation for the above manuscript, I fabricated the thin films, did all the characterizations, and analysed all the data.

Conferences and other participations:

(a) Poster presentation at South African Institute of Physics (SAIP) 67th annual conference

(b) Poster presentation at South African Institute of Physics (SAIP) 68th annual conference.

Student Signature……

Date…….

Supervisor Signature… 

Date… 31 OCTOBER 2024

Co-supervisor Signature……

Date…….

Dedications

This degree is dedicated to my grandparents, Maatseke Magdeline Ntobeng and the late Kgetjepe Ephraim Ntobeng, and my mom Fritah Selekeng Ntobeng.

To my grandparents who taught me resilience, integrity, and kindness, thank you for your endless patience and support. Your wisdom and the values you instilled in me are at the heart of everything I do.

To my mother, whose strength and encouragement have been my constant source of inspiration, thank you for always believing in me.

Together you have been my guiding light, and this degree is a testament to the love and support you have provided.

With all my love, **THIS IS FOR YOU**.

Acknowledgements

- I give all honour and glory to God of Mount Zion for his love and for carrying me through the challenges of this journey.
- A heartfelt thank you to my family for their unconditional love and support.
- I am profoundly grateful to my supervisors Prof Mmantsae Diale and Prof Nolwazi Nombona for their invaluable guidance, patience, and encouragement throughout my research.
- Special thanks to my fellow students Sandile Thubani, Sizwe Sibiya, Alex Sanbito, Beauty Masolo, Thapelo Seimela, Lindiwe Mthimunye, Fokotsa Molefe and others for creating a collaborative and supportive environment. Their feedback and advices have strengthened this work.
- I would like to thank the Microscopy Department for allowing me to use FEG-SEM and HRTEM for analysis.
- I would like to extend my thanks to the Head of Physics Department Prof Chris Theron for providing the resources and facilities necessary for my work.
- I would like to thank National Research Foundation for financial assistance.

Abstract

This study addresses the key components required to enhance the power conversion efficiency of organic solar cells. The first part of the research focuses on incorporating silver nanoparticles into the PEDOT:PSS layer to enhance light absorption. The silver nanoparticles were synthesised using the chemical reduction method. Then incorporated into the PEDOT:PSS liquid to make a blend of PEDOT:PSS and silver nanoparticles. The blend was coated on top of a glass substrate using the spin coating method. Characterisation techniques such as XRD, TEM, SEM, Raman, and UV-vis were used. TEM analysis revealed that the silver nanoparticles synthesised were spherical and ranged in size from 10 to 70 nm. The UV-visible spectroscopy confirmed the presence of the silver nanoparticles, showing an absorption peak at 389 nm. Furthermore, UV-vis analysis was conducted to evaluate the absorption of both the pristine PEDOT:PSS and the PEDOT:PSS with silver nanoparticles. The findings showed an enhanced absorption in the PEDOT:PSS blend with silver nanoparticles, demonstrating that the incorporation of silver nanoparticles into the PEDOT:PSS improved its light absorption properties.

The second part is directed towards fabricating a transparent, flexible, conductive substrate that will serve as an anode for the organic solar cell. Bacterial cellulose synthesised using kombucha tea through static cultivation was combined with polyvinyl alcohol to make flexible, lightweight and transparent substrates. The composite substrates were made conductive by adsorbing multi-walled carbon nanotubes onto the substrate using the adsorption method. Different concentrations of multi-walled carbon nanotubes were explored on the composite films. Characterisation techniques such as UV-vis spectroscopy, SEM, TEM, XRD, TGA and electrical conductivity measurements of the individual components and the final films were assessed. The substrate with a 0.05% concentration of multi-walled carbon nanotubes showed the highest conductivity. The TGA results showed that the addition of polyvinyl alcohol to bacterial cellulose resulted in composite substrates with lower degradation at temperatures 213-467 ℃, as compared to pure bacterial cellulose which is due to the structural degradation of the composite substrates. The UV-vis transmittance spectra indicated that using a higher concentration of multi-walled carbon nanotube dispersion during fabrication resulted in electrically conductive transparent substrates with reduced transparency.

Table of contents

List of Figures

List of Abbreviations

Nanoparticles	NPs
Surface Plasmon Resonance	SPR
Symbiotic Culture of Bacteria and Yeast	SCOBY
Organic Solar Cells	OSCs
Hole Transport Layer	HTL
Electron Transport Layer	ETL
Poly(3,4-ethylene dioxythiophene) polystyrene sulfonate	PEDOT: PSS
Bacterial Cellulose	BC
Bacterial nanofibers	BNF
Polyvinyl alcohol	PVA
Bacterial Cellulose NanoCrystals	BCNCs
Bacterial cellulose nanofibers	BCNF
Deionised water	diH2O
Silver	Ag
Gold	Au
Scanning Electron Microscopy	SEM
Transmission Electron Microscopy	TEM
Thermogravimetric analysis	TGA
Fourier transform infrared	FT-IR
Multiwalled Carbon Nanotubes	MWCNTS
Cetyltrimethylammonium bromide	CTAB

List of Tables

Chapter 1

Introduction

1.1 Background and motivation

Energy is crucial for the stability of our society, without it, our society would face significant challenges and disruptions [1]. The recent electricity outages experienced in South Africa from 2007 to the present, commonly known as load shedding, have emphasised the importance of energy and our heavy dependence on it [2]. Load shedding is a scheduled power outage intended to prevent uncontrollable blackouts due to the inability to meet power demands [3]. These power outages have forced hospitals to operate with minimal care and maintenance, resulting in patient care disruptions [4].

Renewable energy sources such as solar energy stand out as a potential solution for addressing energy-related challenges [5]. It comes from natural resources and has the benefits of being environmentally friendly and sustainable, as it doesn't deplete or destroy the ecosystem [5]. The sun radiates energy at a rate of $3.8 \times 10^{23} kW$, of which the Earth absorbs about $1.8 \times 10^{14} kW$, making solar energy the most abundant renewable energy source [6]. Solar energy technologies like photovoltaics (PV) possess the capacity to fulfil energy demands in an economical, dependable, and environmentally sustainable manner [7, 8].

Photovoltaic (PV) devices like Solar cells directly convert sunlight into electricity [9]. Initially, silicon was used to develop solar cells for commercial purposes, and it remains the most effective material for solar cells used in both home and industrial application [10]. Over 80% of solar panels sold worldwide use these silicon-based solar cells [11]. However, silicon solar cells are associated with relatively high production costs and the availability of certain high purity material used in their manufacturing can be limited [12]. These constraints led to the development of a new generation of solar cells called Organic Solar Cells (OSCs) that is flexible, cost-effective, and lightweight [13].

OSCs are solar cells that uses organic molecules or polymers to convert sunlight into electricity. OSCs consist of multiple layers such as an electrode (anode), Electron Transport Layer (ETL), Hole Transport Layer (HTL), and a second electrode (cathode) [5]. One of the main limitations on the performance of the OSC is the inefficient absorption of incident light [14]. The

efficiency of an OSC is further influenced by factors such as light absorption, charge transport, and the anode [15]. As a result improving the efficiency of the OSCs has been a major focus for years [16,17].

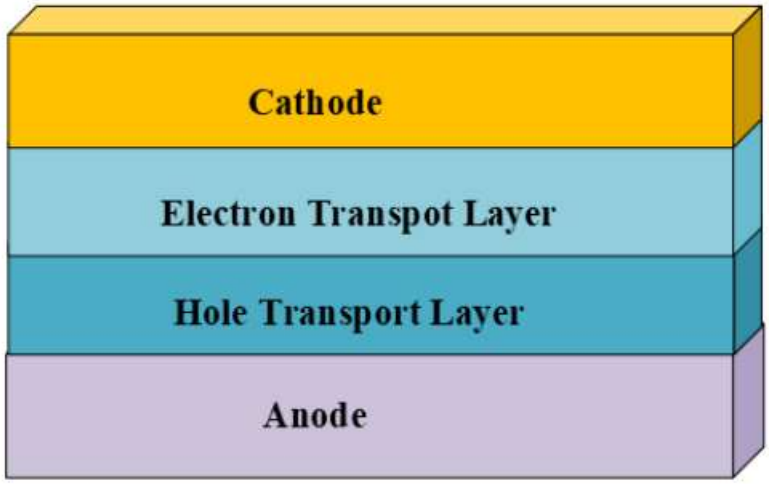

Figure 1.1 The structure of an OSC.

Improving the efficiency of the OSCs has been a major focus for years [14, 15]. The efficiency of an OSC is further influenced by factors such as light absorption, charge transport, and the anode [16]. One of the main limitations on the performance of the OSC is the inefficient absorption of incident light [17]. The development of an adaptable substrate and the integration of metal nanoparticles (NPs) are some of the methods that could enhance light absorption [17]. When metal NPs are integrated into the HTL and ETL layers, various effects help to improve device efficiency. These include better conductivity, enhanced hole injection, scattering, and plasmonic effects [18-20]. In short, these NPs improve the transport layer's conductivity, which improves the device's total performance [21]. The addition of metallic NPs like gold (Au) and silver (Ag) to the Hole Transport Layer (ETL) or Electron Transport Layer (ETL) of OSCs has been reported to drastically improve the PCE of OSCs as shown in Table 1.1 [22].

This study aims to improve the efficiency of OSCs by exploring two methods; synthesizing and integrating Ag NPs into PEDOT:PSS, and fabricating a transparent, conductive, and flexible substrate using Bacterial Cellulose (BC).

The initial approach involves the integration of Ag NPs in the PEDOT:PSS layer, to enhance light absorption. Ag NPs exhibit Localized Surface Plasmon Resonance (LSPR) across a broader wavelength range, extending from the visible to the UV spectrum. The effects of different Ag NPs concentrations on the optical and structural characteristics of PEDOT: PSS

are investigated using X-ray diffraction (XRD), Raman spectroscopy, transmission electron microscopy (TEM), and UV/visible spectroscopy.

The second approach focuses on fabricating a conductive, transparent, and flexible substrate for the OSC by using a composite of bacterial cellulose, polyvinyl alcohol, and multi-walled carbon nanotubes. Currently, the market is dominated by conventional conductive metal oxide substrates like fluorine-doped tin oxide (FTO) and indium tin oxide (ITO). However, these materials come with financial implications, resulting from scarcity of indium, the high costs associated with the necessary deposition processes, and the brittle nature of their ceramic structure [23]. These disadvantages restrict their application in flexible solar cells. Furthermore, the conductivity of ITO significantly decreases after bending, which limits its application in flexible organic electronics [24].

Substrates made of cellulose have the potential to be highly effective substrates for maintaining the components of OSC. These cellulose-based substrates can be processed into flexible, transparent, and electrically conductive films [25]. One significant benefit of using cellulose substrates is their ability to enhance photon absorption at angled incidence. This feature makes cellulose substrates capture light more efficiently than conventional glass substrates [26]. Previous research has focused on the use of plant-derived cellulose to develop cellulose substrates [27-29]. Therefore, this current study reports on the use of bacterial cellulose (BC) to fabricate a flexible, transparent, and electrically conductive substrate, using multiwalled-carbon nanotubes as a conductive material.

Table 1.1: Reports on the improvement of the hole transport layer due to the incorporation of Au and Ag nanoparticles

NPs	Active layer	Size of NP (nm)	Thickness (nm)	Function	FF (%	PCE (%)	Improvement in PCE (%)	Remarks	Ref
Ag	P3HT: PCBM	80	55	HTL	38.80	2.28	2.65	Higher conductivity	[30]
Ag	P3HT: PCBM	20-40	40	HTL	51.20	3.20	3.47	SPR and improved hole collection	[31]
Au	P3HT: PCBM	-	40	HTL	51.50	3.19	3.46	SPR and improved hole collection	[31]
Au	P3HT: PCBM	11± 3	30	HTL	53.30	3.23	4.27	Enhanced extraction of charge in HTL	[32]
Au	P3HT:$PC_{70}BM$	18	40	HTL	69.21	3.51	4.15	SPR and improved hole collection	[33]
	P3HT: PCBM	45± 5	50	HTL	70.32	4.24	5.03	SPR and improved hole collection	[34]
Au	P3HT: PCBM	14 ±4	-	HTL	30.02	1.00	1.66	SPR and improved hole collection	[35]
Au	P3HT:PC_{60} BM	50	30	HTL	66.10	4.14	4.7	Stronger near-field enhancement, thus higher photocurrent output	[36]

1.2 Aim and Objectives

This dissertation aims to enhance the light absorption in the PEDOT: PSS layer and to fabricate a flexible, conductive, and transparent BC substrate for OSC application.

The objectives are:

(a) To synthesise Ag NPs using chemical reduction and study their morphology, structural, and optical properties

(b) To study the changes in PEDOT: PSS due to incorporating plasmonic Ag NPs.

(c) To synthesize Bacterial cellulose using kombucha tea.

(d) To fabricate a substrate using bacterial cellulose and polyvinyl alcohol blend.

(e) To enhance the conductivity of the bacterial cellulose substrate using multi-walled carbon nanotubes.

1.3 Structure of the Dissertation

Chapter 1 Discusses the background and motivation as well as the aim and objectives of the study and the structure of the dissertation.

Chapter 2 Discusses the literature review on different plasmonic NPs, their different properties and significance, cellulose's background, their synthesis, chemical nature, and applications as well as their use in OSCs.

Chapter 3 Details the results on the effect of plasmonic silver nanoparticles in PEDOT: PSS layer.

Chapter 4 Details the results of the fabrication of transparent and flexible bacterial cellulose PVA composite film.

Chapter 5 Details the results of the electrical conductivity of bacterial cellulose/polyvinyl alcohol/ multiwalled carbon nanotube composite films.

Chapter 6 Discusses conclusion and future work.

1.3 References

[1] Burns, M.G., *Managing energy security: an all hazards approach to critical infrastructure*. 2019: Routledge.

[2] Maringa, S.G., *The relationship between reoccurring plant failures and load shedding*. 2017, North-West University (South Africa), Potchefstroom Campus.

[3] Lenoke, M., *The impact of load shedding on the economic growth of South Africa*. 2017, North-West University (South Africa).

[4] Gehringer, C., H. Rode, and M. Schomaker, *The effect of electrical load shedding on pediatric hospital admissions in South Africa.* Epidemiology, 2018. **29**(6): p. 841-847.

[5] Swami, R., *Solar cell.* International Journal of Scientific and Research Publications, 2012. **2**(7): p. 1-5.

[6] Randolph, J., et al., *Fundamentals of Energy Science.* Energy for Sustainability: Foundations for Technology, Planning, and Policy, 2018: p. 95-131.

[7] Shahsavari, A. and M. Akbari, *Potential of solar energy in developing countries for reducing energy-related emissions.* Renewable and Sustainable Energy Reviews, 2018. **90**: p. 275-291.

[8] Kannan, N. and D. Vakeesan, *Solar energy for future world:-A review.* Renewable and sustainable energy reviews, 2016. **62**: p. 1092-1105.

[9] Parida, B., S. Iniyan, and R. Goic, *A review of solar photovoltaic technologies.* Renewable and sustainable energy reviews, 2011. **15**(3): p. 1625-1636.

[10] Goetzberger, A., J. Luther, and G. Willeke, *Solar cells: past, present, future.* Solar energy materials and solar cells, 2002. **74**(1-4): p. 1-11.

[11] Bruton, T., *General trends about photovoltaics based on crystalline silicon.* Solar Energy Materials and Solar Cells, 2002. **72**(1-4): p. 3-10.

[12] Ranabhat, K., et al., *An introduction to solar cell technology.* Journal of Applied Engineering Science, 2016. **14**(4): p. 481-491.

[13] Helgesen, M., R. Søndergaard, and F.C. Krebs, *Advanced materials and processes for polymer solar cell devices.* Journal of Materials Chemistry, 2010. **20**(1): p. 36-60.

[14] Liang, Y., et al., *For the bright future-bulk heterojunction polymer solar cells with power conversion efficiency of 7.4%.* Advanced materials, 2010. **22**(20): p. E135.

[15] Ma, W., et al., *Quantification of nano-and mesoscale phase separation and relation to donor and acceptor quantum efficiency, Jsc, and FF in polymer: fullerene solar cells.* Advanced Materials, 2014. **26**(25): p. 4234-4241.

[16] Kumar, P. and S. Chand, *Recent progress and future aspects of organic solar cells.* Progress in Photovoltaics: Research and applications, 2012. **20**(4): p. 377-415.

[17] Tang, Z., W. Tress, and O. Inganäs, *Light trapping in thin film organic solar cells.* Materials today, 2014. **17**(8): p. 389-396.

[18] Lim, E.L., et al., *A review of recent plasmonic nanoparticles incorporated P3HT: PCBM organic thin film solar cells.* Organic Electronics, 2016. **36**: p. 12-28.

[19] Ali, A., et al., *Improving the efficiency of the organic solar cell (CuPc/C60) via PEDOT: PSS as a photoconductor layer doped by silver nanoparticles.* Results in Physics, 2020. **16**: p. 102819.

[20] Lee, W., et al., *Improving the thermoelectric power factor of CNT/PEDOT: PSS nanocomposite films by ethylene glycol treatment.* Rsc Advances, 2016. **6**(58): p. 53339-53344.

[21] Morfa, A.J., et al., *Plasmon-enhanced solar energy conversion in organic bulk heterojunction photovoltaics.* Applied Physics Letters, 2008. **92**(1).

[22] Xie, F.X., et al., *Improving the efficiency of polymer solar cells by incorporating gold nanoparticles into all polymer layers.* Applied Physics Letters, 2011. **99**(15).

[23] Taha, H., *Optoelectronic and mechanical properties of Sol-Gel derived Multi-Layer ITO thin films improved by elemental doping, Carbon Nanotubes and Nanoparticles*. 2018, Murdoch University.

[24] Zardetto, V., et al., *Substrates for flexible electronics: A practical investigation on the electrical, film flexibility, optical, temperature, and solvent resistance properties.* Journal of Polymer Science Part B: Polymer Physics, 2011. **49**(9): p. 638-648.

[25] Sreekanth, M., A. Rahaman, and T. Sumangala, *Advances in biodegradable polymer nanocomposites for solar cell applications: current status and future directions.* Biodegradable and Biocompatible Polymer Nanocomposites, 2023: p. 397-433.

[26] Subudhi, P. and D. Punetha, *Progress, challenges, and perspectives on polymer substrates for emerging flexible solar cells: A holistic panoramic review.* Progress in Photovoltaics: Research and Applications, 2023. **31**(8): p. 753-789.

[27] Yang, B., et al., *Nature degradable, flexible, and transparent conductive substrates from green and earth-abundant materials.* Scientific Reports, 2017. **7**(1): p. 4936.

[28] Hu, L., et al., *Transparent and conductive paper from nanocellulose fibers.* Energy & Environmental Science, 2013. **6**(2): p. 513-518.

[29] Zhou, Y., et al., *Recyclable organic solar cells on cellulose nanocrystal substrates.* Scientific reports, 2013. **3**(1): p. 1536.

[30] Li, X., et al., *Efficiency enhancement of polymer solar cells with Ag nanoparticles incorporated into PEDOT: PSS layer.* Journal of Materials Science: Materials in Electronics, 2014. **25**: p. 140-145.

[31] Woo, S., et al., *In situ-prepared composite materials of PEDOT: PSS buffer layer-metal nanoparticles and their application to organic solar cells.* Nanoscale Research Letters, 2012. **7**: p. 1-6.

[32] Otieno, F., et al., *Improved efficiency of organic solar cells using Au NPs incorporated into PEDOT: PSS buffer layer.* AIP Advances, 2017. **7**(8).

[33] Wanninayake, A.P. and N. Abu-Zahra, *Enhanced morphological and optoelectronic properties of organic solar cells incorporating CuO, ZnO and Au nanoparticles.* J Mater Environ Sci, 2020. **2508**(11): p. 1874-84.

[34] Wu, J.-L., et al., *Surface plasmonic effects of metallic nanoparticles on the performance of polymer bulk heterojunction solar cells.* ACS nano, 2011. **5**(2): p. 959-967.

[35] Mutuma, B.K., et al., *Effect of gold nanospheres and nanodots on the performance of PEDOT: PSS solar cells.* Journal of Nanoscience and Nanotechnology, 2019. **19**(5): p. 2747-2754.

[36] Li, Q., et al., *Decahedral-shaped Au nanoparticles as plasmonic centers for high performance polymer solar cells.* Organic Electronics, 2017. **43**: p. 33-40.

Chapter 2

Nanoparticles in cellulose-based organic solar cell

2.1 Introduction

In recent years, nanotechnology has emerged as an innovative and interesting topic. Nanotechnology is the study and creation of new materials at the nanoscale level [1]. It is built on the concept that tiny particles, smaller than 100 nanometers (nm) can provide unique properties to structures made from these particles [2]. Multiple industries have used particles in this size range for thousands of years to improve their scientific discoveries [3]. These particles can transform many technology devices, making them more affordable, portable, safe, and easy to use [4]. Figure 2.1 below shows a schematic representation illustrating the methods of synthesising nanoparticles.

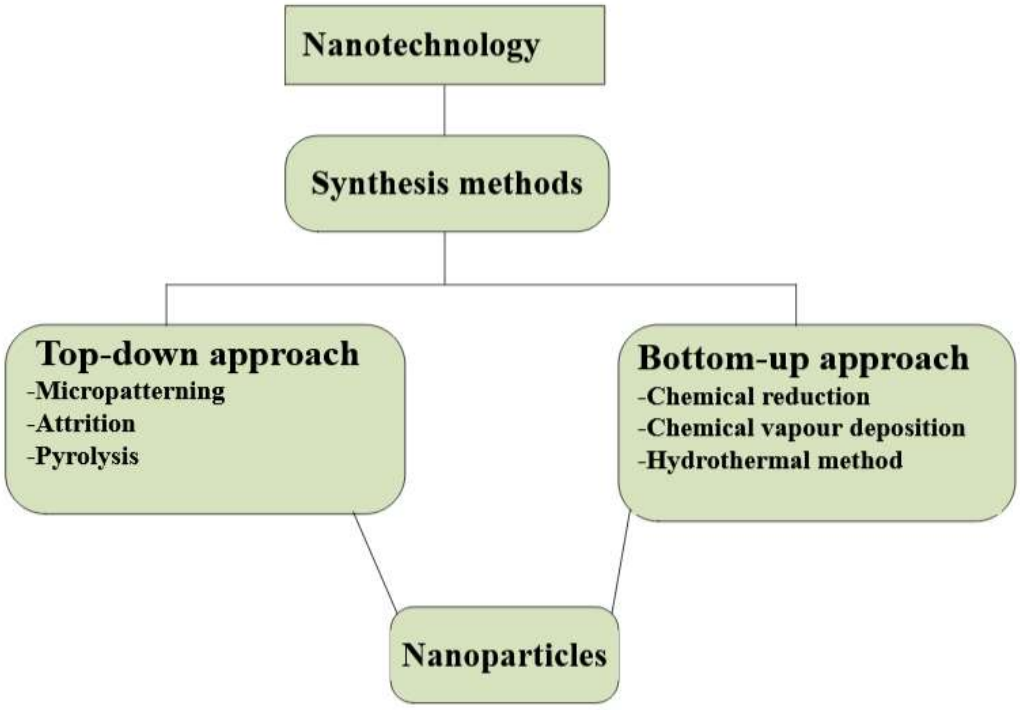

Figure 2.1 Synthesis methods of nanoparticles used in nanotechnology.

2.2 Nanoparticles

Nanoparticles (NPs) are groups of atoms, between 1 and 100 nm in size [5]. Materials such as proteins, polysaccharides, and synthetic polymers can make NPs [6]. The properties of NPs

such as electrical conductivity, mechanical strength, thermal conductivity, and optical properties differ depending on the size of the NPs [7]. Metal NPs such as gold (Au), and silver (Ag) exhibit Surface Plasmon Resonance (SPR) [8]. SPR happens when electrons on the surface of metal NPs get excited by light, at a specific wavelength [8]. NPs have a huge surface area relative to their size. They can take on several dimensional structures, for example, two-dimensional NPs like nanoflakes and nanosheets, zero-dimensional NPs like nanospheres and nanodots, one-dimensional NPs like nanorods, nanowires, and nanotubes [8].

2.2.1 Methods of Producing Nanoparticles

Beginning with Faraday's discovery in 1857, the synthesis of NPs has roughly 167 years of history [9]. The synthesis of NPs is an important part of current scientific research [10]. NPs can be produced in a variety of sizes and shapes [11]. NPs of various shapes such as spheres, rods, and flowers, have been synthesised effectively by precisely managing both their size and shape [12]. Several approaches are currently utilised for the synthesis of NPs.

2.2.1.1 Top-down approaches

A top-down approach involves crushing, milling, and grinding and is a useful method for materials synthesis and particle size reduction [13]. The top-down approach offers simplicity and environmental advantages while being adaptable in its use of different materials and precise in controlling NPs properties [14]. Below are various methods of top-down approaches.

2.2.1.1.1 Micropatterning

Micropatterning is a technique used to synthesise and precisely control how NPs are organised on a substrate [15]. This procedure involves the formation of NPs on a substrate [15]. Among various methods of micropatterning, laser micropatterning is widely favoured when compared to alternative techniques like electro-deposition, chemical vapour deposition, and photolithography [16]. Some of the key advantages of laser micropatterning are high precision and versatility [17]. The following nanoparticles can be produced through micropatterning platinum (Pt), silver (Ag), and gold (Au). Figure 2.2 illustrates a laser micropatterning technique for synthesising Ag NPs through ink synthesis.

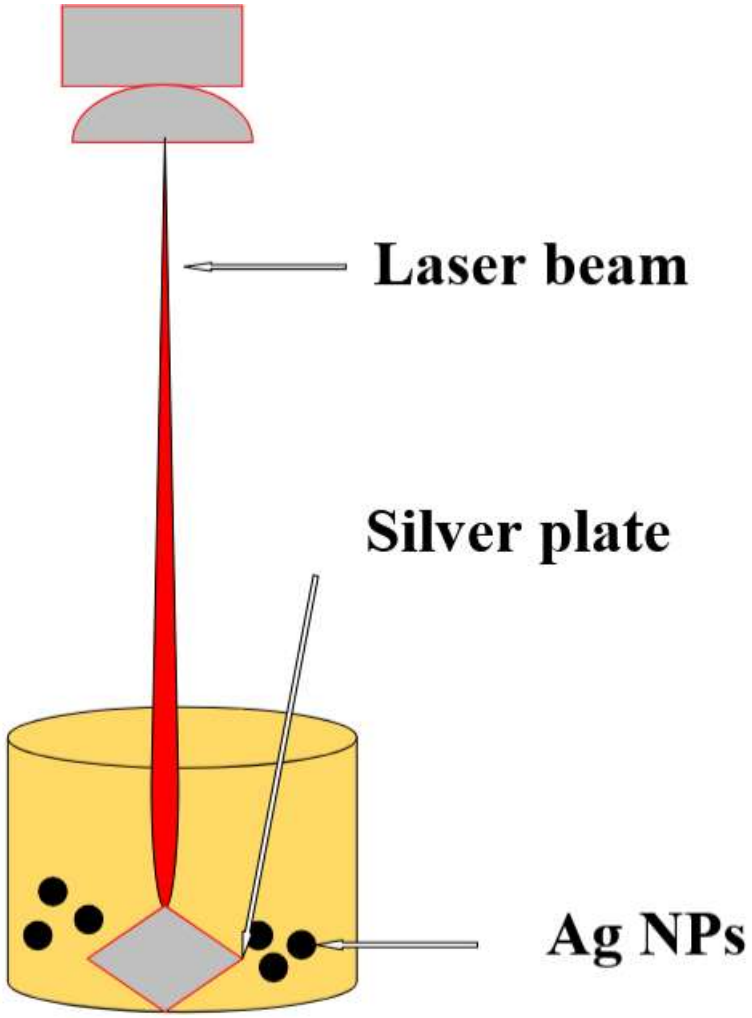

Figure 2.2: Laser micropatterning technique used in the synthesis of silver nanoparticles through ink synthesis [16].

Liu *et al*. synthesised Ag NPs using a laser micropatterning technique. They reported Ag NPs in a size range of 10 to 50 nm and also demonstrated that they were able to achieve precise control over the size and distribution of the NPs by adjusting the laser parameters [18].

2.2.1.1.2 Attrition

Attrition produces NPs in a mill, a mechanical device that uses energy to break down coarse-grained material into nanoscale particles [19]. When materials undergo attrition processes, they usually show a high degree of crystallinity, resulting in particles with diameters ranging from 1 to 10 nm following milling [20]. Some of the factors that affect the size of the particles during the milling process are the speed at which the mill is operated, the size and arrangement of the milling balls, the temperature at which the mill is operated, and the length of the milling

operation [21]. The synthesis of NPs can be accomplished by a variety of ball milling processes, in which the balls contact the bulk material as illustrated in Figure 2.3 [22].

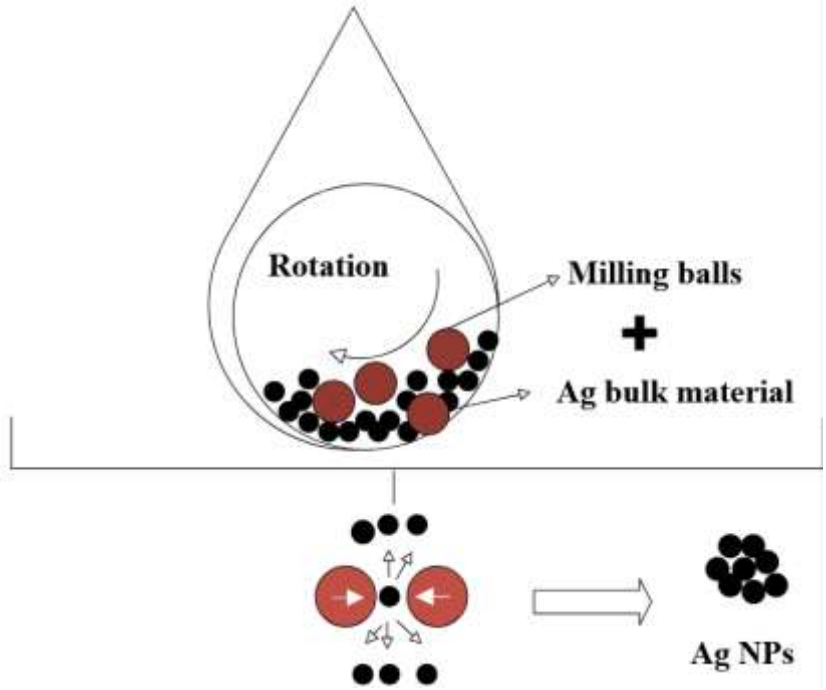

Figure 2.3: Synthesis of Ag nanoparticles through mechanical milling using a planetary milling machine [23].

Khayathi *et al*. produced Ag NPs ranging from 5 to 100 nm in size using a planetary milling machine. They controlled the size distribution by adjusting milling parameters such as rotation speed, milling time, and the ball-to-powder ratio. Their study revealed that longer milling times generally result in smaller particle sizes, but also increase the risk of contamination from the milling media [24].

2.2.1.2 Bottom-up Approaches

In a bottom-up approach, NPs are created by carefully assembling tiny molecules or atoms into larger ones. This can be achieved through evaporation and controlled precipitation also known as crystallization. Depending on the approach used, these processes might occur in tiny droplets or overall the entire solution [28]. Below are various methods associated with the bottom-up approach in the synthesis of NPs.

2.2.1.2.1 Chemical reduction

The chemical reduction synthesis method involves the use of organic and inorganic reducing agents [29]. Generally, a variety of reducing agents, such as sodium citrate ($Na_3C_6H_5O_7$), ascorbate ($C_6H_7O_6$), and sodium borohydride ($NaBH_4$) are employed to reduce Ag ions (Ag^+) in both aqueous and non-aqueous solutions [30]. When Ag^+ are exposed to these reducing agents, they change from Ag^+ to metallic silver (Ag^0), and then the Ag particles aggregate into clusters. Finally, these clusters produce metallic colloidal Ag NPs over time as illustrated in Figure 2.5 [31].

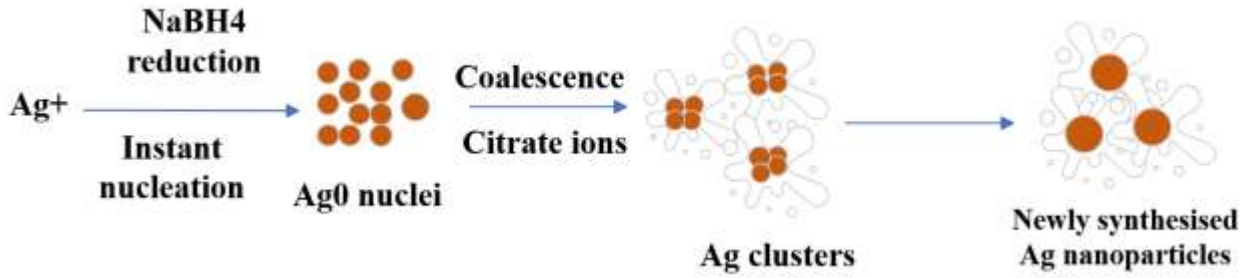

Figure 2.4: Schematic illustration of the controlled sizing of Ag nanoparticles achieved through the chemical reduction method [32].

When using $NaBH_4$ as a reducing agent and water as a solvent, the most commonly utilized capping agents include polyvinyl alcohol, trisodium citrate, and $NaBH_4$ itself [33, 34]. Radziuk *et al*. reported the reduction of $AgNO_3$ using $NaBH_4$ to produce Ag NPs. The produced Ag NPs had sizes ranging from 10 to 50 nm [35]. Kim *et al*. conducted a study where they synthesized spherical Ag NPs. The NPs ranged in size from 5 – 50 nm. They achieved this through the polyol process and a modified precursor injection technique [36].

2.2.1.2.2 Chemical vapour deposition

Chemical Vapor Deposition (CVD) happens when a thin coating of gaseous reactants is applied to a substrate. During this process, a thin layer forms on the surface of the substrate as a result of a chemical reaction that takes place when these gases come into contact with a heated substrate inside a reaction chamber as shown in Figure 2.6 [37]. The CVD method makes it possible to precisely regulate the parameters of the process, which enables the modification of surface properties, orientations of NPs, and crystal structure [38]. It is excellent at guaranteeing material consistency and adherence to the substrate. Moreover, it produces remarkably robust,

uniform, pure, and homogenous NPs [39]. Typical nanoparticles produced using the CVD technique are gold (Au), silver (Ag), nickel (Cu), and platinum (Pt).

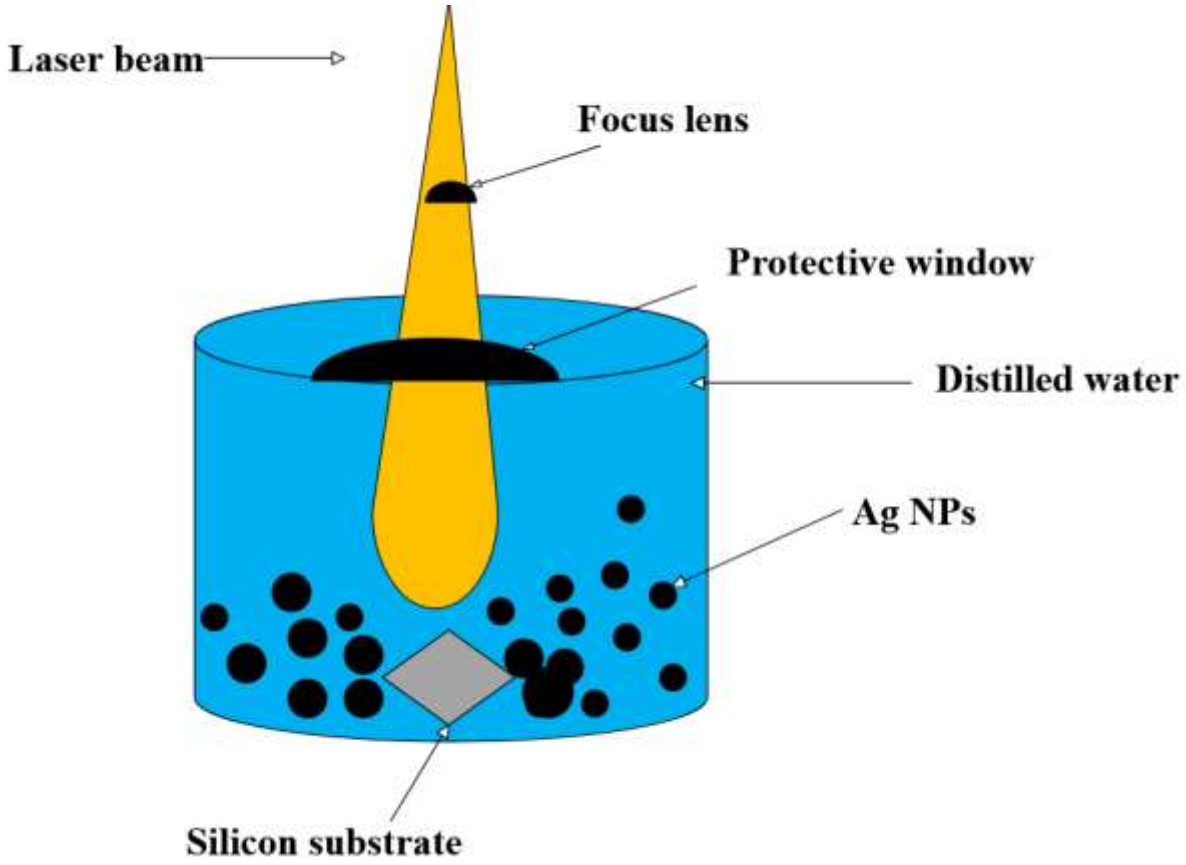

Figure 2.5: Chemical vapour deposition method used for synthesising and depositing Ag NPs on a silicon substrate [40].

2.2.1.2.3 Hydrothermal method

Hydrothermal synthesis takes place when tiny particle deposits are created in a reaction vessel by reacting a solid material with a liquid solution at high temperatures and pressures [41]. The majority of hydrothermal reactions take place within a closed vessel, commonly referred to as an autoclave, a pressure container, or a high-pressure chamber, as illustrated in Figure 2.7 [41]. The hydrothermal method has several benefits such as homogenous precipitation, affordability, environmental friendliness, and scalability [42].

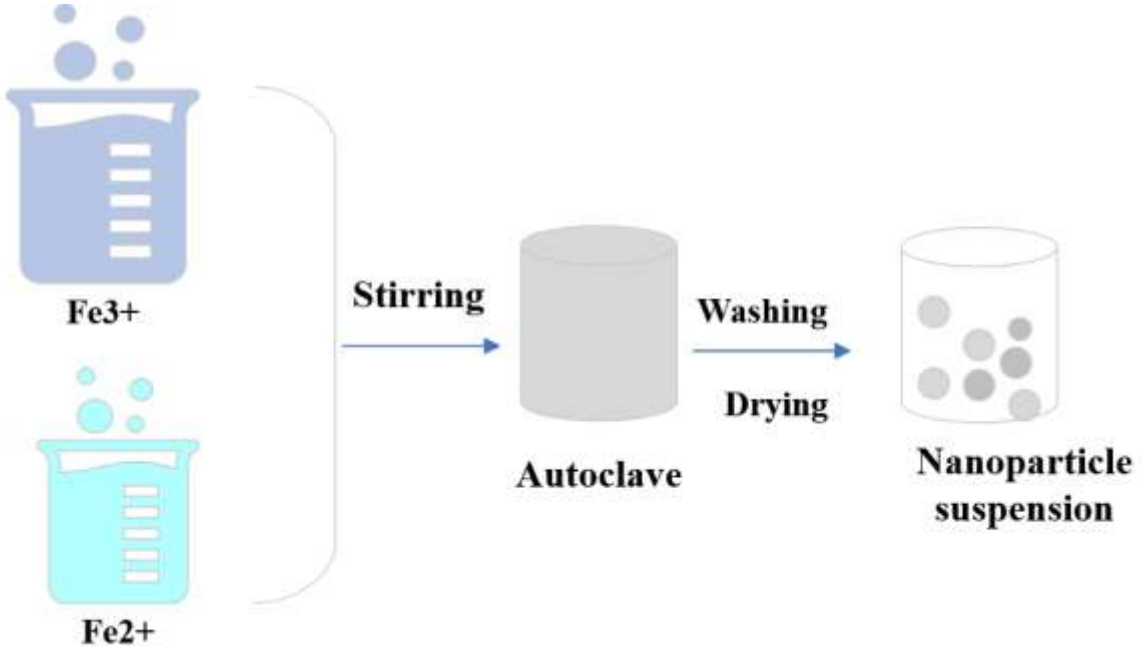

Figure 2.6: A visual representation of the hydrothermal synthesis of NPs [43].

2.2.1.2.4 Microemulsion method

The microemulsion method allows for exact control over the size, shape, structure, homogeneity, and surface area of the particles [44]. In microemulsion, two microemulsions containing the required reactants are mixed to form NPs. The Brownian motion of the micelles interacts with one another, leading to intense collisions that mix the contents of the micellar solution. Reactant mixing requires droplets to undergo fusion-fission processes before chemical reactions may begin. Lots of molecules are produced during the chemical reaction inside the nanodroplets, which starts the nucleus's creation and therefore stimulates the growth of NPs [45].

2.2.1.3 Biological methods

The biological synthesis of NPs provides a more environmentally friendly way to produce NPs [46]. Biological organisms such as bacteria, actinobacteria, yeasts, moulds, algae, and plants are used to synthesise NPs [47]. The following are biological organisms used in the synthesis of NPs.

2.2.1.3.1 Bacteria

Bacteria can easily produce NPs because of their rapid growth, low cost of cultivation, and simplicity in regulating and changing their development environment [46]. Shivaji *et al.* successfully synthesized Ag NPs using a bacteria named *psychrophilic* [48]. Simon *et al.* suggested that a specific gene is accountable for conferring resistance to Ag in bacteria. These bacteria could potentially serve as a substitute for the use of Ag in burn treatments, thereby diminishing the risk of Ag toxicity [49]. Enhanced control over the size of produced NPs can be achieved simply by genetic manipulation of actinobacteria [50].

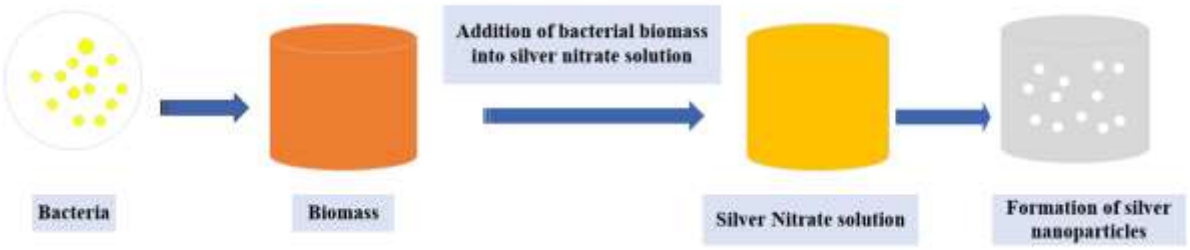

Figure 2.7: Illustration of the synthesis of Ag NPs using bacteria [51].

2.2.1.3.2 Yeasts and fungi

Fungi are known as eukaryotic organisms that live in various settings and are frequently known for their roles as decomposers [52]. Fungi has the ability to simultaneously accumulate and tolerate metals [53]. The filamentous fungus *Fusarium oxysporum* has been widely used as a major species for NP synthesis [54]. Ahmad *et al.* produced highly stable Ag NPs with diameters ranging from 5 to 15 nm by using *Fusarium oxysporum* [55].

Yeast cells use glutathione (GSH) and two types of metal-binding molecules, metallothioneins, and phytochelatins, to remove toxins. These molecules also help create NPs and make sure the complexes are stable in most yeast species [56]. Yeast strains are better than bacteria because they can make lots of NPs easily in the lab, they can make lots of enzymes quickly, and they grow fast with simple food [57]. Geriche *et al.* used the yeast *Pichia jadinii* to produce Au NPs ranging in size from 10 to 100 nm. Figure 2.9 shows the steps involved in producing Ag NPs using fungi.

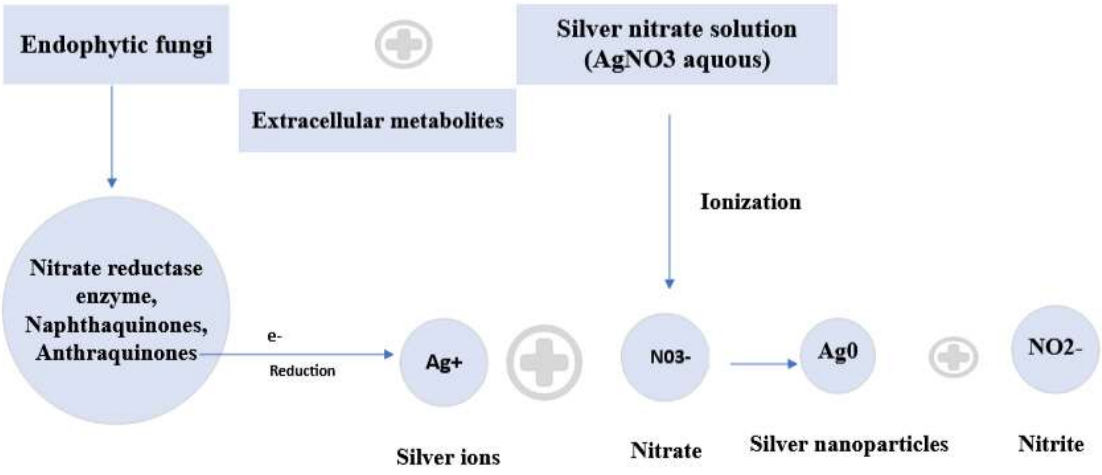

Figure 2.8*:* Diagram representation of the steps involved in producing Ag NPs using fungi [58].

2.2.1.3.3 Algae

Algae are aquatic eukaryotic creatures [59]. The colours, proteins, carbohydrates, lipids, nucleic acids, and secondary metabolites found in algae enable them to degrade metallic salts into NPs [46]. Algae extracts can produce NPs with possible antibacterial qualities when mixed with metal solutions at a particular pH [60]. Ting *et al*. synthesized AuNPs using Chlorella vulgaris, a single-cell green algae from the division Chlorophyta and family Chlorellaceae. The AuNPs produced had a small size (2-10 µm) and a spherical shape along with the lack of flagella, making it a good candidate for nanoparticle synthesis [61].

2.2.1.3.4 Plants

A wide range of plant components, such as fruits, leaves, stems, flowers and roots, have been used in the synthesis of NPs [62]. Plants produce a large amount of H^+ ions during glycolysis in addition to Nicotinamide Adenine Dinucleotide (NAD), a powerful reducing agent. This phenomenon is helpful for the production of Ag NPs [63]. In a study investigating different antioxidant components in extracts from pomegranate, turmeric, blueberries, and blackberries, it was found that pomegranate can produce Au and Ag NPs that are more uniform in size and shape, with sizes between 20 and 500 nm. These NPs could be used in antioxidant therapy and

cancer management [64]. Badri *et al*. reported the synthesis of Ag and Au NPs, using coriander leaf extract as the reducing agent. The coriander leaf extract generated NPs with diameters varying from 6.75 to 57.91 nm [65]. Ria *et al*. have reported the creation of triangular Au and Ag shell NPs through the reduction of Au^{+} with lemongrass extract [66].

Figure 2.9: Mapping of environmentally friendly synthesis method using plant leaves for the production of NPs [67].

2.2.1.3.5 Enzymes

Enzymes are preferred in NPs synthesis due to their well-defined structure and high purity [68]. Enzymes are utilized to stimulate growth on solid substrates in the production of Ag NPs, guaranteeing purity and accuracy in the process. A sulfite reductase enzyme from *Escherichia coli* that had been isolated using ion exchange chromatography was used to make a cell-free extract that could be used to make Au NPs. When applied to human pathogenic fungi, these Au NPs demonstrated antifungal capabilities [68, 69]. Raju et al. successfully synthesized Au-Ag bimetallic nanoparticles using macerase enzyme as a reducing agent. The synthesis was conducted at two different temperatures, 80°C and 90°C [70].

2.2.1.3.6 Vitamins

The synthesis of silver and palladium nano-spheres, nanowires, and nanorods has been achieved in an environmentally friendly manner by using vitamin B2 as a capping and reducing agent [71]. When generating nanowires and nanorods, vitamin B2 functions as a reducing agent in two different ways. This strategy is notable in the field of green nanotechnology because it investigates the effects of natural substances on different tumour cells while using them to further scientific goals [71]. Nadagouda *et al*. reported a green chemistry approach using vitamin B2 as a reducing agent and capping agent in the synthesis of Ag nanospheres, nanowires, and nanorods at room temperature. The average particle size of the nanoparticles was found to be 6.1 ± 0.1 nm [72].

2.3 Application of nanoparticles

2.3.1 Cosmetics

Ag NPs scatter light, When Ag NPs are integrated into cosmetic products like creams or serums, these NPs contribute to achieving a brighter and more uniform complexion resulting in skin looking more radiant and reducing the appearance of dullness or uneven skin tone [73]. Kokura *et al*. conducted a study that highlights the impressive potential of silver nanoparticles as effective preservatives in cosmetic products [74].

2.3.2 Electronics

The increased demand for larger and brighter screens in modern televisions and computer monitors drives the widespread use of NPs in display technology. Ag nanowires and spheres have been used as pastes and inks in printed circuit board manufacturing, as well as electrodes for thin-film transistors [75]. They find use in data storage devices, optoelectronics, and intercalation-based battery materials [76]. Cho *et al*. demonstrated that Ag NPs boosted the performance of surface-enhanced blue LEDs. The efficiency of the SP-enhanced blue LED improved by 72% when Ag NPs were bonded to the p-GaN layer [77].

2.3.3 Medicine

Through the use of NPs in drug delivery, nanotechnology has improved the medical industry. Drug delivery to particular cells can now be done on a targeted basis [78]. Ag is used in some

Ayurvedic (traditional Indian medicine) procedures. A common recommendation is to use Ag to improve memory. In some medication formulations, Au is added to support a child's cognitive health [79]. Peng *et al*. developed a biosensor device using gold nanoparticles that can identify lung cancer by analysing an individual's exhaled breath [80].

2.3.4 Food

Improvements in food production, processing, preservation, and packaging are made possible by NPs. In a food packaging process, the incorporation of a nanocomposite coating allows for the direct introduction of antimicrobial substances onto the surface of the coated film. In the canola oil production industry, an example involves the utilisation of nano drops, an additive specifically designed to facilitate the transfer of vitamins and minerals within the food [81]. Shafrina *et al*. explored the effects of combining LDPE film packaging with Ag NPs and a modified atmosphere on the shelf life of chicken breast fillets [82].

2.3.5 Construction

Construction processes have been improved by NPs, which has made them safer, quicker, and more inexpensive. For instance, when NPs are incorporated into conventional concrete, it enhances its mechanical properties and durability. Similarly, the inclusion of haematite (Fe_2O_3) NPs leads to increased strength in the concrete [83]. Hegazy *et al*. studied the impact of colloidal copper nanoparticles as an additive in corrosion-resistant coatings for steel [84].

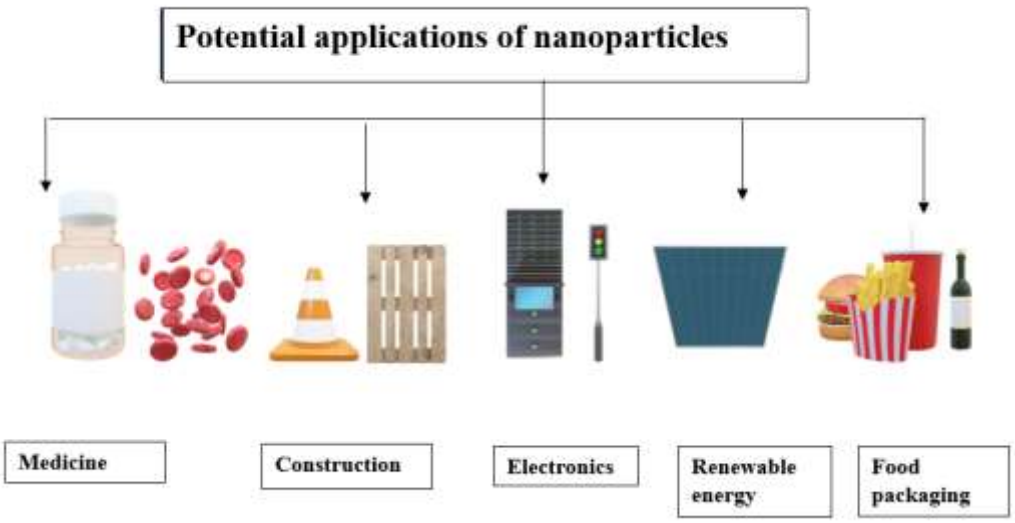

Figure 2.10: Various potential uses of NPs in different sectors [85].

2.4 Architecture of Organic Solar Cell

OSCs are fabricated using the spin coating method. OSC device is made up of multiple layers as illustrated in Figure 2.12. It consists of two electrodes, one optically transparent as an anode, and a metal as a cathode.

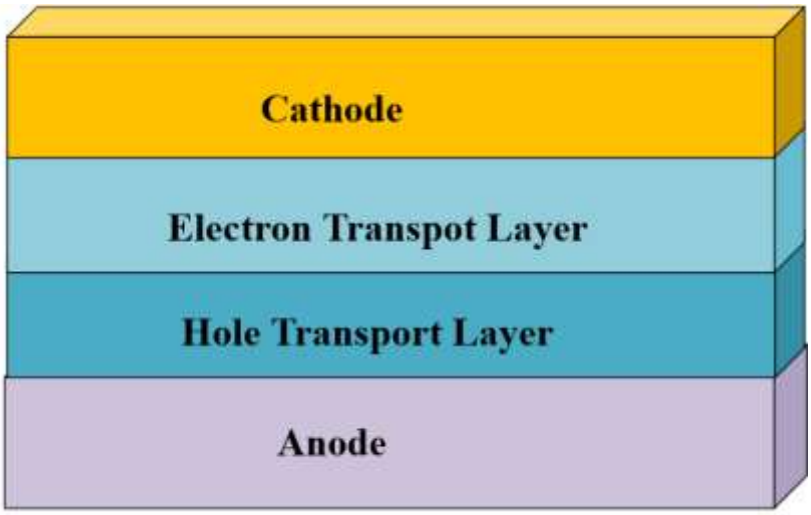

Figure 2.11 Architecture of an Organic Solar Cell.

2.4.1 Anode

The Anode is a layer which gets exposed to light within the device. Indium Tin Oxide (ITO) is a front electrode depending on architecture. The layer performs two functions; it gathers the photogenerated holes as an anode and serves as a transparent window layer [86]. Sungo *et al* used ITO as an electrode for their organic solar cell structured as ITO/PEDOT: PSS-Ag NPs/P3HT: PCBM/LiF which demonstrated an 8% increase in their power conversion efficiency primarily due to the increased surface roughness of the PEDOT: PSS [87].

2.4.2 Hole Transport Layer

Poly(3,4-ethylene dioxythiophene) polystyrene sulfonate (PEDOT: PSS) is frequently used as an HTL due to its ability to improve hole collection at the ITO electrode [88]. Gao *et al* used PEDOT: PSS as their HTL for their Bulk heterojunction organic solar cell with the structure ITO/PEDOT: PSS-Au NPs/P3HT: PCBM/Al It has been found that the power conversion efficiency increased from 3.50% to 4.07% after incorporating the 60 nm Au NPs [89].

2.4.3 Electron transport layer

Electron Transport Layer (ETL) is a layer in which charge carriers are generated as a result of most incident light absorption, P3HT: PCBM is usually used as an ETL [90]. The ETL extracts and transports electrons while also preventing the undesired movement of hole carriers [91]. Paul *et al*. used P3HT: PCBM as an electron transport layer for their organic solar cell [92].

2.4.4 Cathode

This is the Top layer which is usually made of Ag, Au, or another metal with a suitable work function to facilitate improved electron transport. Xiong *et al* used aluminium as a cathode in their organic solar cell fabrication The PSC devices with architecture ITO/PEDOT: PSS (with or without Ag NPs)/P3HT: PCBM/Al The results showed that power conversion efficiency increased from 2.28 to 2.65 % when 0.1 wt% Ag NPs was incorporated in PEDOT: PSS layer [93].

2.5 Nanoparticles in Organic Solar Cells

The incorporation of metal NPs into OSCs has the potential to improve power conversion efficiency (PCE) [94]. Recent studies have shown that the most commonly used light-trapping strategy involves integrating metallic NPs into the ETL/HTL layer of an OSC [95]. The improvements in these layers enhance the extraction of charge carriers toward the electrodes and reduce the recombination of charge carriers at the interface between the cathode ITO and the photoactive layer. This could enhance the performance of the OSCs [95].

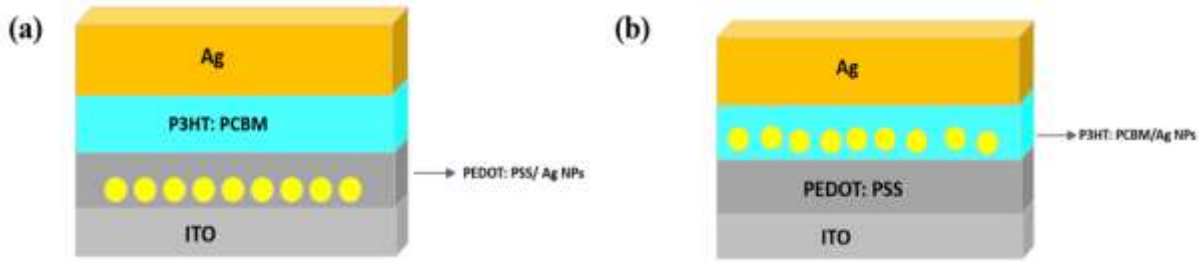

Figure 2.12 The device structure of an OSC with Ag NPs incorporated in the (a) HTL layer (PEDOT: PSS), and (b) ETL layer (P3HT: PCBM).

In their study, Lee *et al*. explored the incorporation of Ag NPs ranging in diameter from 10 to 100 nm into the PEDOT: PSS layer of the OSC. As a result, the PCE of the solar cell reached a notable 8.6% [96]. Otieno *et al*. investigated the plasmonic resonance of Au inside the

PEDOT: PSS layer. Their findings showed a 32.4% improvement in PCE [97]. Goru *et al*. incorporated Ag and Au NPs in the P3HT: PCBM layer to enhance light absorption, the NPs varied in size from 10 to 50 nm. The PCE was found to be 4.21% and 4.44%, respectively [91].

2.6 Cellulose

The most widely used polymer on earth is cellulose, produced by plants, algae, and certain bacterial species [98]. Plants and marine organisms like tunicates, have large amounts of cellulose while algae, fungi, and bacteria have smaller amounts of cellulose [99]. Cellulose exists in two forms, cellulose I and II, and is the primary constituent of all-natural fibers [98]. Many hydroxyl groups in the cellulose chain cause a network of intra- and inter-molecular linkages [100]. Hydroxyl groups in cellulose help form hydrogen bonds, creating a micro-fibrillated structure of crystalline and amorphous parts [101]. Nishiyama *et al*. conducted a study on the structure of cellulose, revealing that it has two crystal phases, namely Iα and Iβ. The Iα crystal phase has been identified in the cell walls of certain algae organisms, whereas the Iβ crystal phase is predominantly found in cotton, wood, and ramie fibers [102].

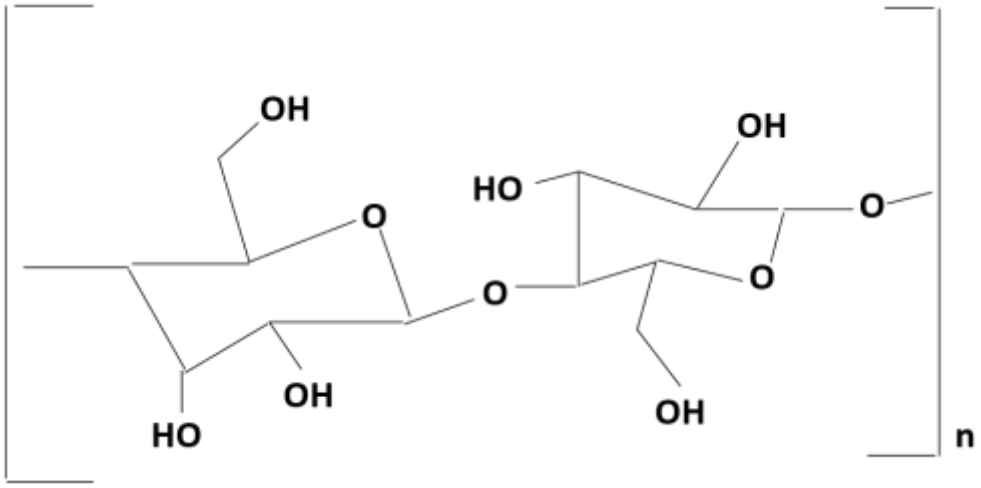

Figure 2.13: Chemical structure of cellulose [103].

2.6.1 Bacterial cellulose

In 1886, Brown studied the existence of cellulose generated by bacteria, called bacterial cellulose (BC) [104]. BC can be found in various sources, such as vinegar, fruits, vegetables, and alcoholic beverages [105]. BC is produced as a thick white gel by an acetic acid bacteria

called *Gluconaceto bacter xylinus.* BC possess the following characteristics, 60-90% cellulose crystallinity, high purity, high mechanical strength, full biocompatibility, and a high degree of polymerization [106, 107]. Although the chemical structure of BC is similar to that of plant-based cellulose, BC has many benefits because its formation is not dependent on climate, happens readily, and is not associated with hemicellulose, lignin, or pectin [108].

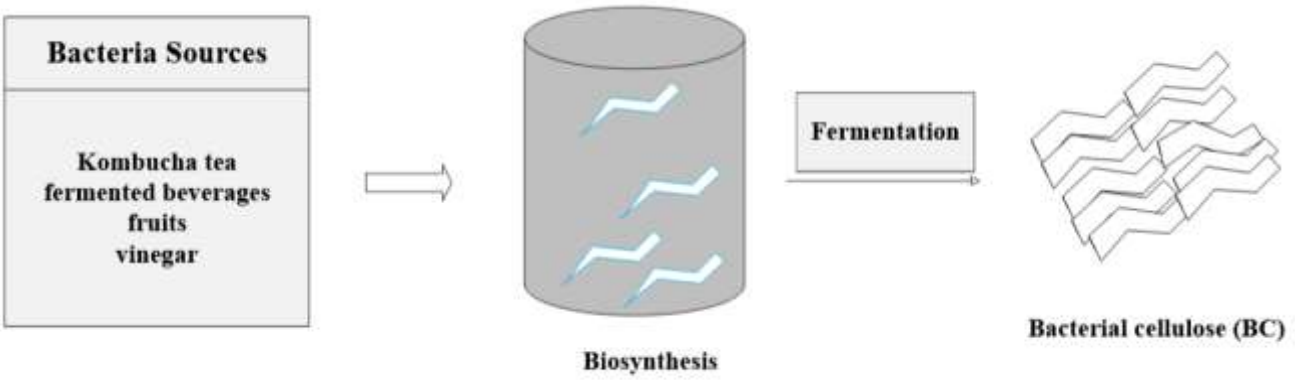

Figure 2.14: Biosynthesis of bacterial cellulose.

Guzel *et al*. explored the use of citrus peels for the production of BC. The results demonstrated that the BC had favourable properties, making it a potential material for various industrial applications [104]. Ha *et al*. investigated the use of waste beer culture broth to produce BC. They found that the waste beer culture broth provided an effective and low-cost medium for BC production [109]. It is challenging for BC to produce a transparent film with sufficient strength due to the hydrogen bonds that hold the BC fibers together. Therefore BC tends to be produced to a nanoscale size through acid hydrolysis, enzymatic hydrolysis and tempo-mediated oxidation methods [110].

2.6.1.1 Production of Bacterial Cellulose NanoCrystals (BCNCs)

The BC can be processed into bacterial cellulose nanocrystals (BCNCs) by enzymatic and acid hydrolysis methods. BCNCs, also known as nanowhiskers, are rigid and resemble an extended crystal rod. BCNC usually exhibits lengths between 50 and 600 nm and widths between 3 and 50 nm [99].

2.6.1.1.1 Acid hydrolysis

The acid hydrolysis is a process that converts fine pulp bacterial fibers into BCNCs, by breaking down the fiber's amorphous domains and splitting down hydrogen bonds [111]. The two primary reactions that occur during this process are the breakdown of glycosidic bonds

and the addition of ester groups to the surface hydroxy (OH) groups [112]. Cellulose chains shorten due to the rapid breakdown of glycosidic bonds, which primarily occurs in the less organised regions of cellulose. This leads to the retention of mostly crystalline regions in the cellulose structure [113].

Different kinds of acid treatments, such as hydrochloric (HCl), sulfuric (H_2SO_4), and phosphoric acids (H_3PO_4), have been used to produce BCNCs [114]. Every treatment adds unique functional groups to the surface of the fibres, affecting their colloidal stability. HCl acid-generated BCNCs have suboptimal colloidal stability, while H_2SO_4 acid-produced BCNCs have highly stable colloidal dispersion due to negatively charged sulfate ester groups [115]. The important condition in the hydrolysis process is to preserve the basic structure of the BC backbone [116]. Three primary factors influence the outcome of the acid hydrolysis reaction; the duration of the reaction, the temperature, and the concentration of acid used [117].

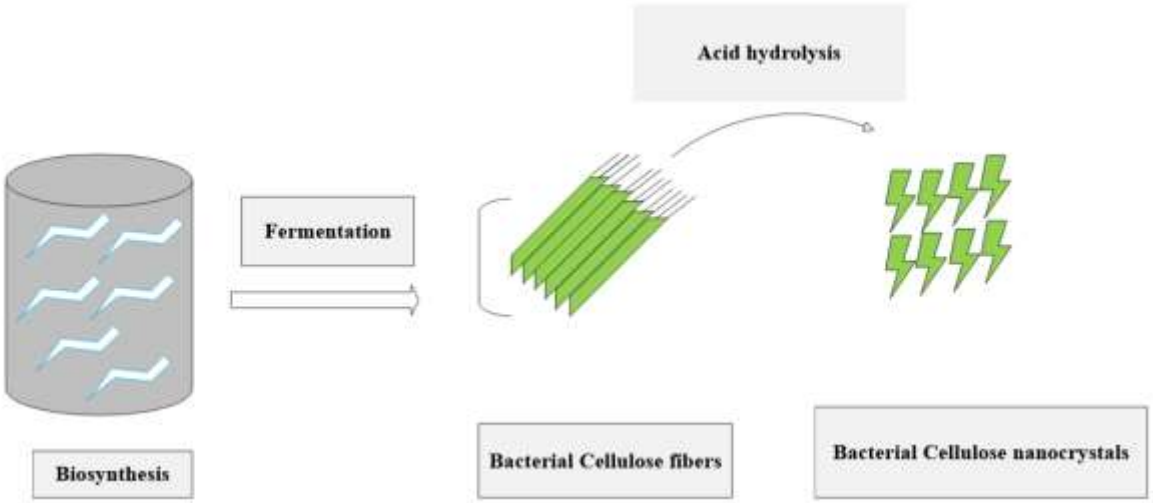

Figure 2.15: Isolation of cellulose nanocrystals derived from bacterial cellulose through acid hydrolysis.

The optimization of reaction conditions is crucial for controlling the yield and properties of BCNCs in the isolation process [117]. A fine balance is required to get the best hydrolysis since too long of a reaction time breaks down the cellulose fiber, while short of a period results in big, insoluble fibers and aggregates [118]. Le Gars *et al*. reported a high yield amount of BCNCs. Their method involved several stages, including the mechanical pre-treatment of cellulose, controlled acid hydrolysis, and subsequent post-treatment steps such as homogenization and ultrasonication. By applying these methods together, they were able to produce a high yield of BCNCs [117].

2.6.1.1.2 Enzymatic hydrolysis

Enzymatic hydrolysis is a heterogeneous reaction where enzymes such as endoglucanase, cellobiohydrolase, and cellobiase work together to break down hydrogen bonds that connect BC fibers to produce BCNCs [119, 120]. Enzymatic treatment does not modify the structure of BC since it targets the amorphous areas of BC fibers, leading to lower energy requirements for homogenization or microfluidization [121]. The following factors influence the enzymatic process; temperature, the enzyme concentration, and the length of time the enzyme is active [122]. Higher enzyme concentrations generate an expected increase in enzyme adsorption onto the BC fibers, which in turn increases the rate of enzymatic hydrolysis [123]. George *et al*. reported BCNCs with a size range of 100–300 nm in length and 10–15 nm in diameter after a 12-hour enzymatic treatment [122].

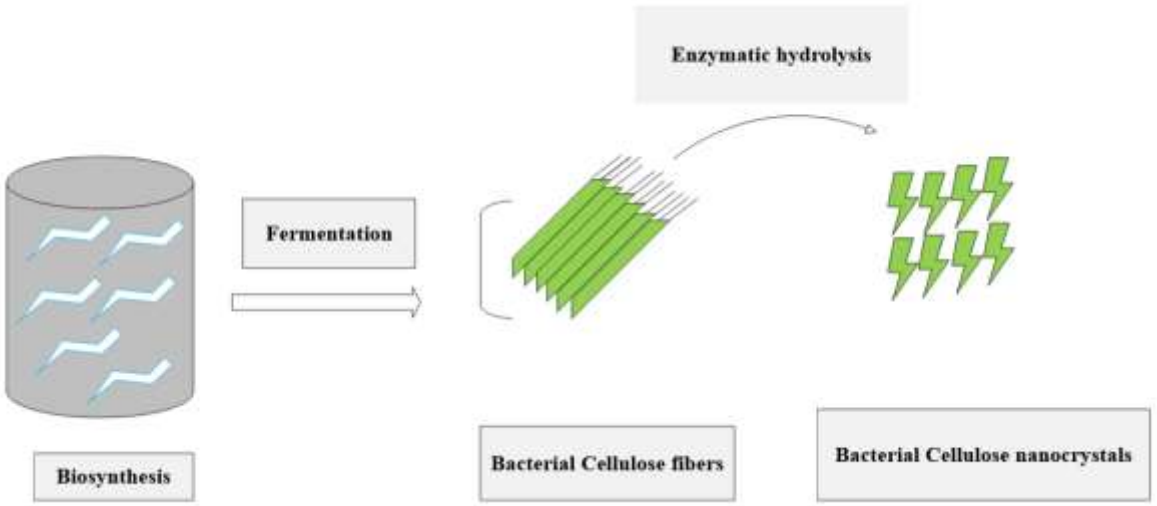

Figure 2.16: Isolation of cellulose nanocrystals from bacterial cellulose by enzymatic hydrolysis.

2.6.1.2 Production of cellulose nanofibers

Bacterial cellulose nanofibers (BCNF) are a collection of elongated nanofibers. Fibers made of BC are elastic and bound together, with a large surface area [124]. BCNFs are isolated through the Tempo-mediated oxidation method.

2.6.1.2.1 TEMPO-mediated oxidation

The TEMPO-mediated oxidation process weakens the hydrogen bonding between BC fibers, separating them into BCNFs [125]. This is achieved by mitigating the negative or positive charges on the fiber surfaces and introducing carboxylic (COOH) groups to the BC fibers during the oxidation process [126]. TEMPO-mediated oxidation is recognized for its ability to decrease the thermal stability of nanocellulose and improve the colloidal stability of the resulting cellulose nanofibrils [127]. Zheng *et al*. reported BCNFs with reduced thermal stability when produced using the TEMPO-mediated oxidation method [128]. Saito *et al*. reported that individual BCNFs can be prepared by TEMPO-mediated oxidation followed by mild mechanical treatment. They also reported BCNFs with reduced thermal stability [129].

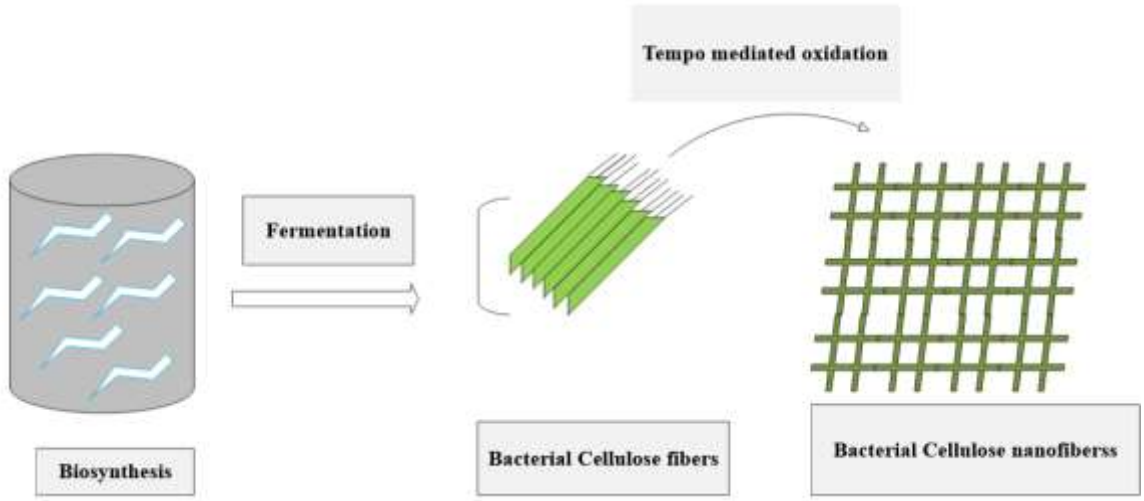

Figure 2.17: Isolation of cellulose nanofibers from bacterial cellulose by tempo-mediated oxidation.

2.7 The use of BC in organic solar cell

Recently a transparent cellulose film has emerged as a novel green material to improve the efficiency of organic solar cells [130-132]. The primary goals for developing novel organic solar cell substrates are to use materials that are transparent, flexible, thermally stable, sustainable, and recyclable. These properties have been proven in transparent cellulose films [133-136]. Hu *et al*. created cellulose film with a light transmission of over 90%, showcasing its application in solar cells for the first time. Their research revealed that optical transparency is positively impacted by a transparent CNF film's width [137]. Solar cell that is made up of

flexible substrate have several advantages over traditional rigid solar cell made of glass or silicon wafer substrates. These include being thin, lightweight, portable, easy to integrate over curved or uneven surfaces and less risk of breaking [138] and having superior mechanical properties attributed to a higher packing density of fibers [139]

Research has indicated that the utilisation of polymers in solar cell devices can increase light absorption in the module. This could increase the power conversion efficiency of solar cells [140]. Zhou *et al*. recently demonstrated a cellulose-based organic solar cell with a 2.7% power conversion efficiency. However, the random distribution of cellulose fibers in the film caused light scattering and reduced transmittance [141].

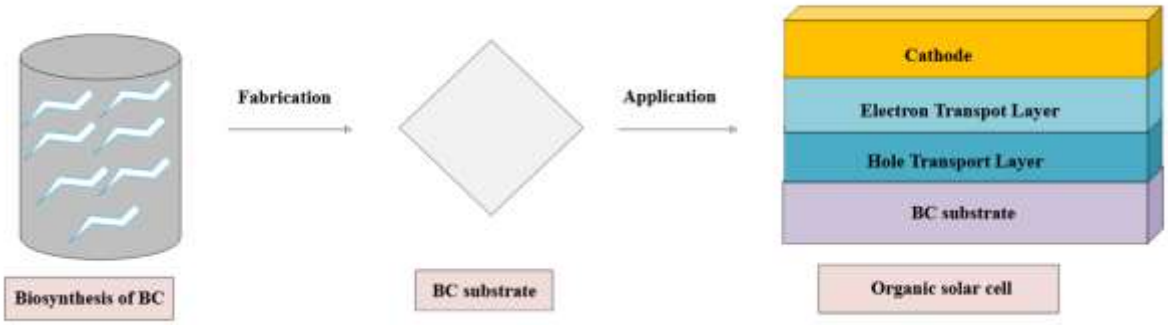

Figure 2.18: Schematic of cellulose-based organic solar cell.

2.10 References

[1] Castro Alarcon, N., et al., *Antibacterial activity of nanoparticles of titanium dioxide, intrinsic and doped with indium and iron.* 2016.

[2] Poole, C.P. and F.J. Owens, *Introduction to nanotechnology.* 2003.

[3] Biswas, P. and C.-Y. Wu, *Nanoparticles and the environment.* Journal of the air & waste management association, 2005. **55**(6): p. 708-746.

[4] Aithal, P. and S. Aithal, *Ideal technology concept & its realization opportunity using nanotechnology.* International Journal of Application or Innovation in Engineering & Management (IJAIEM), 2015. **4**(2): p. 153-164.

[5] Murthy, S.K., *Nanoparticles in modern medicine: state of the art and future challenges.* International journal of nanomedicine, 2007. **2**(2): p. 129-141.

[6] Mohanraj, V. and Y. Chen, *Nanoparticles-a review.* Tropical journal of pharmaceutical research, 2006. **5**(1): p. 561-573.

[7] Jambhulkar, S., et al., *Nanoparticle Assembly: From Self-Organization to Controlled Micropatterning for Enhanced Functionalities.* Small, 2023: p. 2306394.

[8] Doria, G., et al., *Noble metal nanoparticles for biosensing applications.* Sensors, 2012. **12**(2): p. 1657-1687.

[9] Bonardd, S., C. Quezada, and A. Leiva, *The role of polymers in the synthesis of noble metal nanoparticles: a review.* Journal of nanoscience and nanotechnology, 2017. **17**(1): p. 87-114.

[10] Vadlapudi, V., et al., *Synthesis of green metallic nanoparticles (NPs) and applications.* Orient. J. Chem, 2013. **29**(4): p. 1589-1595.

[11] Brust, M., et al., *Synthesis of thiol-derivatised gold nanoparticles in a two-phase liquid–liquid system.* Journal of the Chemical Society, Chemical Communications, 1994(7): p. 801-802.

[12] Kim, S.-W., et al., *Synthesis of monodisperse palladium nanoparticles.* Nano Letters, 2003. **3**(9): p. 1289-1291.

[13] Almásy, L., et al., *Wet milling versus co-precipitation in magnetite ferrofluid preparation.* Journal of the Serbian Chemical Society, 2015. **80**(3): p. 367-376.

[14] Priyadarshana, G., et al., *Synthesis of magnetite nanoparticles by top-down approach from a high purity ore.* Journal of Nanomaterials, 2016. **16**(1): p. 317-317.

[15] Yang, W., et al., *Recent advance in cell patterning techniques: Approaches, applications and future prospects.* Sensors and Actuators A: Physical, 2022. **333**: p. 113229.

[16] Park, S., et al., *Micropatterning of metal nanoparticle ink by laser-induced thermocapillary flow.* Nanomaterials, 2018. **8**(9): p. 645.

[17] Yoon, S.H., et al., *Sintering and consolidation of silver nanoparticles printed on polyimide substrate films.* Macromolecular Research, 2009. **17**: p. 568-574.

[18] Liu, Y.-K. and M.-T. Lee, *Laser direct synthesis and patterning of silver nano/microstructures on a polymer substrate.* ACS applied materials & interfaces, 2014. **6**(16): p. 14576-14582.

[19] DeCastro, C.L. and B.S. Mitchell, *Nanoparticles from mechanical attrition.* Synthesis, functionalization, and surface treatment of nanoparticles, 2002. **5**.

[20] Gleiter, H. *Nanocrystalline materials*. in *Advanced Structural and Functional Materials: Proceedings of an International Seminar Organized by Deutsche Forschungsanstalt für Luft-und Raumfahrt (DLR), Köln, June 1991*. 1991. Springer.

[21] Yadav, T.P., R.M. Yadav, and D.P. Singh, *Mechanical milling: a top down approach for the synthesis of nanomaterials and nanocomposites.* Nanoscience and Nanotechnology, 2012. **2**(3): p. 22-48.

[22] Koch, C.C. and J. Whittenberger, *Mechanical milling/alloying of intermetallics.* Intermetallics, 1996. **4**(5): p. 339-355.

[23] de Lima Barizão, A.C., et al., *Nanomagnetic approach applied to microalgae biomass harvesting: advances, gaps, and perspectives.* Environmental Science and Pollution Research, 2021. **28**: p. 44795-44811.

[24] Khayati, G. and K. Janghorban, *The nanostructure evolution of Ag powder synthesized by high energy ball milling.* Advanced Powder Technology, 2012. **23**(3): p. 393-397.

[25] Panchasara, H. and N. Ashwath, *Effects of pyrolysis bio-oils on fuel atomisation—a review.* Energies, 2021. **14**(4): p. 794.

[26] Majerič, P. and R. Rudolf, *Advances in ultrasonic spray pyrolysis processing of noble metal nanoparticles.* Materials, 2020. **13**(16): p. 3485.

[27] Lee, J.-H., *Technological realization of semiconducting metal oxide–based gas sensors*, in *Gas Sensors Based on Conducting Metal Oxides*. 2019, Elsevier. p. 167-216.

[28] Chan, H.-K. and P.C.L. Kwok, *Production methods for nanodrug particles using the bottom-up approach.* Advanced drug delivery reviews, 2011. **63**(6): p. 406-416.

[29] Iravani, S., et al., *Synthesis of silver nanoparticles: chemical, physical and biological methods.* Research in pharmaceutical sciences, 2014. **9**(6): p. 385.

[30] Evanoff, D.D. and G. Chumanov, *Size-controlled synthesis of nanoparticles. 2. Measurement of extinction, scattering, and absorption cross sections.* The Journal of Physical Chemistry B, 2004. **108**(37): p. 13957-13962.

[31] Wiley, B., et al., *Shape-controlled synthesis of metal nanostructures: the case of silver.* Chemistry–A European Journal, 2005. **11**(2): p. 454-463.

[32] Sharma, R., S. Dewanjee, and C. Kole, *Utilization of nanoparticles for plant protection.* Plant Nanotechnology: Principles and Practices, 2016: p. 305-327.

[33] He, J. and T. Kunitake, *Formation of silver nanoparticles and nanocraters on silicon wafers.* Langmuir, 2006. **22**(18): p. 7881-7884.

[34] Seo, D., et al., *The preparation of hydrophobic silver nanoparticles via solvent exchange method.* Colloids and Surfaces A: Physicochemical and Engineering Aspects, 2008. **313**: p. 158-161.

[35] Radziuk, D., et al., *Stabilization of silver nanoparticles by polyelectrolytes and poly (ethylene glycol).* Macromolecular rapid communications, 2007. **28**(7): p. 848-855.

[36] Kim, D., S. Jeong, and J. Moon, *Synthesis of silver nanoparticles using the polyol process and the influence of precursor injection.* Nanotechnology, 2006. **17**(16): p. 4019.

[37] Bhaviripudi, S., et al., *CVD synthesis of single-walled carbon nanotubes from gold nanoparticle catalysts.* Journal of the American Chemical Society, 2007. **129**(6): p. 1516-1517.

[38] Pottathara, Y.B., et al., *Synthesis and processing of emerging two-dimensional nanomaterials*, in *Nanomaterials synthesis*. 2019, Elsevier. p. 1-25.

[39] Abid, N., et al., *Synthesis of nanomaterials using various top-down and bottom-up approaches, influencing factors, advantages, and disadvantages: A review.* Advances in Colloid and Interface Science, 2022. **300**: p. 102597.

[40] Fernández-Arias, M., et al., *Synthesis and deposition of Ag nanoparticles by combining laser ablation and electrophoretic deposition techniques.* Coatings, 2019. **9**(9): p. 571.

[41] Li, J., Q. Wu, and J. Wu, *Synthesis of Nanoparticles via Solvothermal and Hydrothermal Methods 12.* 2016.

[42] Jamkhande, P.G., et al., *Metal nanoparticles synthesis: An overview on methods of preparation, advantages and disadvantages, and applications.* Journal of drug delivery science and technology, 2019. **53**: p. 101174.

[43] Lester, E., et al., *Reaction engineering: The supercritical water hydrothermal synthesis of nano-particles.* The Journal of Supercritical Fluids, 2006. **37**(2): p. 209-214.

[44] Hu, A., Z. Yao, and X. Yu, *Phase behavior of a sodium dodecanol allyl sulfosuccinic diester/n-pentanol/methyl acrylate/butyl acrylate/water microemulsion system and preparation of acrylate latexes by microemulsion polymerization.* Journal of applied polymer science, 2009. **113**(4): p. 2202-2208.

[45] Malik, M.A., M.Y. Wani, and M.A. Hashim, *Microemulsion method: A novel route to synthesize organic and inorganic nanomaterials: 1st Nano Update.* Arabian journal of Chemistry, 2012. **5**(4): p. 397-417.

[46] Nadaroglu, H., A.A. GÜNGÖR, and İ. Selvi, *Synthesis of nanoparticles by green synthesis method.* International Journal of Innovative Research and Reviews, 2017. **1**(1): p. 6-9.

[47] Nadaroglu, H., H. Onem, and A. Alayli Gungor, *Green synthesis of Ce2 O3 NPs and determination of its antioxidant activity.* IET nanobiotechnology, 2017. **11**(4): p. 411-419.

[48] Shivaji, S., S. Madhu, and S. Singh, *Extracellular synthesis of antibacterial silver nanoparticles using psychrophilic bacteria.* Process Biochemistry, 2011. **46**(9): p. 1800-1807.

[49] Silver, S., *Bacterial silver resistance: molecular biology and uses and misuses of silver compounds.* FEMS microbiology reviews, 2003. **27**(2-3): p. 341-353.

[50] Bhosale, R.S., et al., *Biosynthesis, characterization and study of antimicrobial effect of silver nanoparticles by Actinomycetes spp.* Int. J. Curr. Microbiol. Appl. Sci, 2015. **2**: p. 144-151.

[51] Rafique, M., et al., *A review on green synthesis of silver nanoparticles and their applications.* Artificial cells, nanomedicine, and biotechnology, 2017. **45**(7): p. 1272-1291.

[52] Taylor, D.L. and R.L. Sinsabaugh, *The soil fungi: occurrence, phylogeny, and ecology.* Soil microbiology, ecology, and biochemistry, 2015. **4**: p. 77-109.

[53] Sastry, M., et al., *Biosynthesis of metal nanoparticles using fungi and actinomycete.* Current science, 2003: p. 162-170.

[54] Boroumand Moghaddam, A., et al., *Nanoparticles biosynthesized by fungi and yeast: a review of their preparation, properties, and medical applications.* Molecules, 2015. **20**(9): p. 16540-16565.

[55] Ahmad, A., et al., *Extracellular biosynthesis of silver nanoparticles using the fungus Fusarium oxysporum.* Colloids and surfaces B: Biointerfaces, 2003. **28**(4): p. 313-318.

[56] Gericke, M. and A. Pinches, *Microbial production of gold nanoparticles.* Gold bulletin, 2006. **39**: p. 22-28.

[57] Kumar, D., et al., *Biosynthesis of silver nanoparticles from marine yeast and their antimicrobial activity against multidrug resistant pathogens.* Pharmacologyonline, 2011. **3**: p. 1100-1111.

[58] Guilger-Casagrande, M. and R.d. Lima, *Synthesis of silver nanoparticles mediated by fungi: a review.* Frontiers in bioengineering and biotechnology, 2019. **7**: p. 287.

[59] Karaduman, I., et al., *Green synthesis of γ-Fe 2 O 3 nanoparticles for methane gas sensing.* Journal of Materials Science: Materials in Electronics, 2017. **28**: p. 16094-16105.

[60] Siddiqi, K.S. and A. Husen, *Fabrication of metal and metal oxide nanoparticles by algae and their toxic effects.* Nanoscale research letters, 2016. **11**: p. 1-11.

[61] Ting, Y., W. Teo, and C. Soh, *Gold uptake by Chlorella vulgaris.* Journal of applied phycology, 1995. **7**: p. 97-100.

[62] Iravani, S., *Green synthesis of metal nanoparticles using plants.* Green Chemistry, 2011. **13**(10): p. 2638-2650.

[63] Ahmad, N., et al., *Biosynthesis of silver nanoparticles from Desmodium triflorum: a novel approach towards weed utilization.* Biotechnology research international, 2011. **2011**.

[64] Nadagouda, M.N., et al., *Synthesis of silver and gold nanoparticles using antioxidants from blackberry, blueberry, pomegranate, and turmeric extracts.* ACS Sustainable Chemistry & Engineering, 2014. **2**(7): p. 1717-1723.

[65] Narayanan, K.B. and N. Sakthivel, *Coriander leaf mediated biosynthesis of gold nanoparticles.* Materials Letters, 2008. **62**(30): p. 4588-4590.

[66] Gan, P.P. and S.F.Y. Li, *Potential of plant as a biological factory to synthesize gold and silver nanoparticles and their applications.* Reviews in Environmental Science and Bio/Technology, 2012. **11**: p. 169-206.

[67] Goutam, S.P., et al., *Green synthesis of nanoparticles and their applications in water and wastewater treatment.* Bioremediation of Industrial Waste for Environmental Safety: Volume I: Industrial Waste and Its Management, 2020: p. 349-379.

[68] Adelere, I.A. and A. Lateef, *A novel approach to the green synthesis of metallic nanoparticles: the use of agro-wastes, enzymes, and pigments.* Nanotechnology Reviews, 2016. **5**(6): p. 567-587.

[69] Gholami-Shabani, M., et al., *Enzymatic synthesis of gold nanoparticles using sulfite reductase purified from Escherichia coli: a green eco-friendly approach.* Process Biochemistry, 2015. **50**(7): p. 1076-1085.

[70] Raju, D., R. Mendapara, and U.J. Mehta, *Protein mediated synthesis of Au–Ag bimetallic nanoparticles.* Materials Letters, 2014. **124**: p. 271-274.

[71] Nadagouda, M.N. and R.S. Varma, *Green and controlled synthesis of gold and platinum nanomaterials using vitamin B2: density-assisted self-assembly of nanospheres, wires and rods.* Green Chemistry, 2006. **8**(6): p. 516-518.

[72] Nadagouda, M.N. and R.S. Varma, *Green synthesis of Ag and Pd nanospheres, nanowires, and nanorods using vitamin B 2: Catalytic polymerisation of aniline and pyrrole.* Journal of Nanomaterials, 2008.

[73] Gupta, V., et al., *Nanotechnology in cosmetics and cosmeceuticals—A review of latest advancements.* Gels, 2022. **8**(3): p. 173.

[74] Kokura, S., et al., *Silver nanoparticles as a safe preservative for use in cosmetics.* Nanomedicine: Nanotechnology, Biology and Medicine, 2010. **6**(4): p. 570-574.

[75] Tate, J., et al., *Anodization and microcontact printing on electroless silver: Solution-based fabrication procedures for low-voltage electronic systems with organic active components.* Langmuir, 2000. **16**(14): p. 6054-6060.

[76] Tolaymat, T.M., et al., *An evidence-based environmental perspective of manufactured silver nanoparticle in syntheses and applications: a systematic review and critical appraisal of peer-reviewed scientific papers.* Science of the total environment, 2010. **408**(5): p. 999-1006.

[77] Saini, I. and Y.M. Himanshi, *Optoelectronic and sensing applications of plasmonic silver nanoparticles.* International Journal of Technical Research & Science, 2020: p. 2454-2024.

[78] Ganesh, K., D. Archana, and K. Preeti, *Review article on targeted polymeric nanoparticles: an overview.* Am. J. Adv. Drug Deliv, 2013. **3**(3): p. 196-215.

[79] Shinde, N.C., N.J. Keskar, and P.D. Argade, *Nanoparticles: Advances in drug delivery systems.* Res. J. Pharm. Biol. Chem. Sci, 2012. **3**(1): p. 922-929.

[80] Peng, G., et al., *Diagnosing lung cancer in exhaled breath using gold nanoparticles.* Nature nanotechnology, 2009. **4**(10): p. 669-673.

[81] Laad, M. and V.K.S. Jatti, *Titanium oxide nanoparticles as additives in engine oil.* Journal of King Saud University-Engineering Sciences, 2018. **30**(2): p. 116-122.

[82] Azlin-Hasim, S., et al., *Effects of a combination of antimicrobial silver low density polyethylene nanocomposite films and modified atmosphere packaging on the shelf life of chicken breast fillets.* Food Packaging and Shelf Life, 2015. **4**: p. 26-35.

[83] Nazari, A. and S. Riahi, *RETRACTED: The effects of SiO2 nanoparticles on physical and mechanical properties of high strength compacting concrete*. 2011, Elsevier.

[84] Hegazy, M., et al., *Influence of copper nanoparticles capped by cationic surfactant as modifier for steel anti-corrosion paints.* Egyptian Journal of Petroleum, 2013. **22**(4): p. 549-556.

[85] Khan, Y., et al., *Classification, synthetic, and characterization approaches to nanoparticles, and their applications in various fields of nanotechnology: A review.* Catalysts, 2022. **12**(11): p. 1386.

[86] Dholam, R.S., *Development of Solar Sensitive Thin Film for Water Splitting and Water Heating Using Solar Concentrator*. 2010, University of Trento.

[87] Woo, S., et al., *In situ-prepared composite materials of PEDOT: PSS buffer layer-metal nanoparticles and their application to organic solar cells.* Nanoscale Research Letters, 2012. **7**: p. 1-6.

[88] Nardes, A.M., R.A. Janssen, and M. Kemerink, *A morphological model for the solvent-enhanced conductivity of PEDOT: PSS thin films.* Advanced Functional Materials, 2008. **18**(6): p. 865-871.

[89] Gao, H., et al., *Plasmon enhanced polymer solar cells by spin-coating Au nanoparticles on indium-tin-oxide substrate.* Applied Physics Letters, 2012. **101**(13).

[90] Kumar, P. and S. Chand, *Recent progress and future aspects of organic solar cells.* Progress in Photovoltaics: Research and applications, 2012. **20**(4): p. 377-415.

[91] Gollu, S.R., et al., *Incorporation of silver and gold nanostructures for performance improvement in P3HT: PCBM inverted solar cell with rGO/ZnO nanocomposite as an electron transport layer.* Organic Electronics, 2016. **29**: p. 79-87.

[92] Shaw, P.E., A. Ruseckas, and I.D. Samuel, *Exciton diffusion measurements in poly (3-hexylthiophene).* Advanced Materials, 2008. **20**(18): p. 3516-3520.

[93] Li, X., et al., *Efficiency enhancement of polymer solar cells with Ag nanoparticles incorporated into PEDOT: PSS layer.* Journal of Materials Science: Materials in Electronics, 2014. **25**: p. 140-145.

[94] Srivastava, A., D. Samajdar, and D. Sharma, *Plasmonic effect of different nanoarchitectures in the efficiency enhancement of polymer based solar cells: A review.* Solar Energy, 2018. **173**: p. 905-919.

[95] Liao, H.-C., et al., *Nanoparticle-tuned self-organization of a bulk heterojunction hybrid solar cell with enhanced performance.* ACS nano, 2012. **6**(2): p. 1657-1666.

[96] Baek, S.-W., et al., *Plasmonic forward scattering effect in organic solar cells: a powerful optical engineering method.* Scientific reports, 2013. **3**(1): p. 1726.

[97] Otieno, F., et al., *Improved efficiency of organic solar cells using Au NPs incorporated into PEDOT: PSS buffer layer.* AIP Advances, 2017. **7**(8).

[98] Thakur, V.K., M.K. Thakur, and R.K. Gupta, *Graft copolymers of natural fibers for green composites.* Carbohydrate polymers, 2014. **104**: p. 87-93.

[99] Habibi, Y., L.A. Lucia, and O.J. Rojas, *Cellulose nanocrystals: chemistry, self-assembly, and applications.* Chemical reviews, 2010. **110**(6): p. 3479-3500.

[100] Pinkert, A., et al., *Ionic liquids and their interaction with cellulose.* Chemical reviews, 2009. **109**(12): p. 6712-6728.

[101] KROON-BATENBURG, L.J., J. Kroon, and M. Northolt, *Chain modulus and intramolecular hydrogen bonding in native and regenerated cellulose fibres.* Polymer communications (Guildford), 1986. **27**(10): p. 290-292.

[102] Nishiyama, Y., et al., *Crystal structure and hydrogen bonding system in cellulose Iα from synchrotron X-ray and neutron fiber diffraction.* Journal of the American Chemical Society, 2003. **125**(47): p. 14300-14306.

[103] Chandra, R. and R. Rustgi, *Biodegradable polymers.* Progress in polymer science, 1998. **23**(7): p. 1273-1335.

[104] Brown, A.J., *XLIII.—On an acetic ferment which forms cellulose.* Journal of the Chemical Society, Transactions, 1886. **49**: p. 432-439.

[105] Wang, J., J. Tavakoli, and Y. Tang, *Bacterial cellulose production, properties and applications with different culture methods–A review.* Carbohydrate polymers, 2019. **219**: p. 63-76.

[106] Klemm, D. and B. Heublein, *h.-P. Fink, A. Bohn.* Angew. Chem. Int. Ed, 2005. **44**: p. 3358-3393.

[107] Kim, D.-Y., Y. Nishiyama, and S. Kuga, *Surface acetylation of bacterial cellulose.* Cellulose, 2002. **9**: p. 361-367.

[108] Shi, Z., et al., *Utilization of bacterial cellulose in food.* Food hydrocolloids, 2014. **35**: p. 539-545.

[109] Ha, J.H., et al., *Production of bacterial cellulose by a static cultivation using the waste from beer culture broth.* Korean Journal of Chemical Engineering, 2008. **25**: p. 812-815.

[110] Wu, C.-N. and K.-C. Cheng, *Strong, thermal-stable, flexible, and transparent films by self-assembled TEMPO-oxidized bacterial cellulose nanofibers.* Cellulose, 2017. **24**(1): p. 269-283.

[111] Chieng, B.W., et al., *Isolation and characterization of cellulose nanocrystals from oil palm mesocarp fiber.* Polymers, 2017. **9**(8): p. 355.

[112] Gunathilake, T.M.S.U., et al., *Investigations on the interactions of proteins with nanocellulose produced via sulphuric acid hydrolysis.* International journal of biological macromolecules, 2021. **193**: p. 1522-1531.

[113] Vanderfleet, O.M. and E.D. Cranston, *Production routes to tailor the performance of cellulose nanocrystals.* Nature Reviews Materials, 2021. **6**(2): p. 124-144.

[114] Almeida, T., et al., *Bacterial nanocellulose toward green cosmetics: Recent progresses and challenges.* International Journal of Molecular Sciences, 2021. **22**(6): p. 2836.

[115] Grishkewich, N., et al., *Recent advances in the application of cellulose nanocrystals.* Current Opinion in Colloid & Interface Science, 2017. **29**: p. 32-45.

[116] Noremylia, M., M.Z. Hassan, and Z. Ismail, *Recent advancement in isolation, processing, characterization and applications of emerging nanocellulose: A review.* International Journal of Biological Macromolecules, 2022. **206**: p. 954-976.

[117] Le Gars, M., et al., *Cellulose nanocrystals: From classical hydrolysis to the use of deep eutectic solvents*. 2020: IntechOpen London, UK.

[118] Islam, M.T., et al., *Preparation of nanocellulose: A review.* AATCC Journal of Research, 2014. **1**(5): p. 17-23.

[119] Satyamurthy, P., et al., *Preparation and characterization of cellulose nanowhiskers from cotton fibres by controlled microbial hydrolysis.* Carbohydrate Polymers, 2011. **83**(1): p. 122-129.

[120] Phanthong, P., et al., *Nanocellulose: Extraction and application.* Carbon Resources Conversion, 2018. **1**(1): p. 32-43.

[121] Yang, X., et al., *Surface and interface engineering for nanocellulosic advanced materials.* Advanced Materials, 2021. **33**(28): p. 2002264.

[122] George, J., K. Ramana, and A.S. Bawa, *Bacterial cellulose nanocrystals exhibiting high thermal stability and their polymer nanocomposites.* International Journal of Biological Macromolecules, 2011. **48**(1): p. 50-57.

[123] Reshmy, R., et al., *Nanocellulose-based products for sustainable applications-recent trends and possibilities.* Reviews in Environmental Science and Bio/Technology, 2020. **19**: p. 779-806.

[124] Miyashiro, D., R. Hamano, and K. Umemura, *A review of applications using mixed materials of cellulose, nanocellulose and carbon nanotubes.* Nanomaterials, 2020. **10**(2): p. 186.

[125] Indarti, E., R. Rohaizu, and W. Wanrosli, *Silylation of TEMPO oxidized nanocellulose from oil palm empty fruit bunch by 3-aminopropyltriethoxysilane.* International journal of biological macromolecules, 2019. **135**: p. 106-112.

[126] Xu, R., et al., *Valorization of enzymatic hydrolysis residues from corncob into lignin-containing cellulose nanofibrils and lignin nanoparticles.* Frontiers in Bioengineering and Biotechnology, 2021. **9**: p. 677963.

[127] Zheng, D., et al., *Isolation and characterization of nanocellulose with a novel shape from walnut (Juglans regia L.) shell agricultural waste.* Polymers, 2019. **11**(7): p. 1130.

[128] Shaheen, T.I. and H.E. Emam, *Sono-chemical synthesis of cellulose nanocrystals from wood sawdust using acid hydrolysis.* International journal of biological macromolecules, 2018. **107**: p. 1599-1606.

[129] Saito, T., et al., *Homogeneous suspensions of individualized microfibrils from TEMPO-catalyzed oxidation of native cellulose.* Biomacromolecules, 2006. **7**(6): p. 1687-1691.

[130] Preston, C., et al., *Silver nanowire transparent conducting paper-based electrode with high optical haze.* Journal of Materials Chemistry C, 2014. **2**(7): p. 1248-1254.

[131] Fang, Z., et al., *Novel nanostructured paper with ultrahigh transparency and ultrahigh haze for solar cells.* Nano letters, 2014. **14**(2): p. 765-773.

[132] Jia, C., et al., *Scalable, anisotropic transparent paper directly from wood for light management in solar cells.* Nano Energy, 2017. **36**: p. 366-373.

[133] Kim, T.S., et al., *Solution-processible polymer solar cells fabricated on a papery substrate.* physica status solidi (RRL)–Rapid Research Letters, 2012. **6**(1): p. 13-15.

[134] Wang, F., et al., *Papery solar cells based on dielectric/metal hybrid transparent cathode.* Solar Energy Materials and Solar Cells, 2010. **94**(7): p. 1270-1274.

[135] Lee, C.-P., et al., *A paper-based electrode using a graphene dot/PEDOT: PSS composite for flexible solar cells.* Nano Energy, 2017. **36**: p. 260-267.

[136] Hu, W., et al., *Transparent and hazy all-cellulose composite films with superior mechanical properties.* ACS Sustainable Chemistry & Engineering, 2018. **6**(5): p. 6974-6980.

[137] Hu, L., et al., *Transparent and conductive paper from nanocellulose fibers.* Energy & Environmental Science, 2013. **6**(2): p. 513-518.

[138] Roldán-Carmona, C., et al., *Flexible high efficiency perovskite solar cells.* Energy & Environmental Science, 2014. **7**(3): p. 994-997.

[139] Zhu, H., et al., *Transparent paper: fabrications, properties, and device applications.* Energy & Environmental Science, 2014. **7**(1): p. 269-287.

[140] Yao, Y., et al., *Light management in plastic–paper hybrid substrate towards high-performance optoelectronics.* Energy & Environmental Science, 2016. **9**(7): p. 2278-2285.

[141] Zhou, Y., et al., *Recyclable organic solar cells on cellulose nanocrystal substrates.* Scientific reports, 2013. **3**(1): p. 1

Chapter 3: Effect of plasmonic silver nanoparticles in PEDOT: PSS layer

3.1 Introduction

Conducting polymers (CPs) are widely recognised as innovative materials that merge the specific parameters of metals, which include electrical and optical properties and charge transfer [1]. Poly (3,4-ethylene dioxythiophene): Poly (styrene sulfonate) (PEDOT:PSS) is a conductive polymer that offers excellent transparency, low density, and high thermal stability [2]. PEDOT:PSS is made up of negatively charged insulating PSS and positively charged conjugated PEDOT [3]. This is a deep blue microdispersion that is normally used as a hole transport layer (HTL) in solar cell devices [4]. PEDOT:PSS films can be fabricated using the PEDOT: PSS aqueous dispersion through solution-processing methods such as spin coating, slot die coating, and spray deposition [5].

Plasmonic nanoparticles with tunable optical resonance properties improve the absorption of light by amplifying photocurrents in Organic Solar Cells (OSCs) through light-trapping methods [1]. Surface plasmon resonance (SPR) is a behaviour at the frequency of the dipole surface plasmon caused by the surface's confinement of the nanoparticle's (NPs) internal conduction electrons and the creation of a powerful restorative force [6]. Plasmons can result from the interaction of conduction electrons and electromagnetic waves with metallic NPs (localized plasmon) [7]. In OSCs, various metal NPs including platinum (Pt), gold (Au), and silver (Ag) are being researched since they can improve light absorption [8].

The application of SPR derived from metal NPs integrated into the PEDOT:PSS layer has been reported [9, 10]. Plasmonic enhancement is regarded to be one of the best techniques due to its simple method, high efficiency, and the ability to modify the size, shape, and composition of the particles to manipulate the plasmon absorption wavelength [11]. The metallic NPs are encapsulated within a matrix of a dielectric material like polymer (PEDOT:PSS) since their dipole surface plasmon frequency enables them to interact with light very intensely due to the NPs' collective electron velocity being excited [6].

Most of the research on the improvement of OSCs using SPR in devices has centered on metal NPs of various sizes doped in the active layer. Therefore, in this study, we demonstrate a doping

method for adding Ag NPs to the HTL of OSCs to improve the absorption of light. We also investigate Ag NPs impact on our PEDOT:PSS film's structural and optical properties.

3.2 Materials and Instrumentation

3.2.1 Chemicals

Silver nitrate ($AgNO_3$), Trisodium citrate ($Na_3C_6H_5O_7$), Ethanol amine(C_7H_7NO), and Sodium borohydride ($NaBH_4$) were obtained from Sigma Aldrich. Glass substrates and PEDOT: PSS were obtained from Ossila.

3.2.2 Characterization Techniques

Field emission gun transmission electron microscope (FEG-TEM, Jeol 2100) and field emission scanning electron microscope (FE-SEM Zeiss SEM Microscope Crossbeam-540) were used to characterise the morphology of the samples. The optical absorbance was measured using an Agilent Cary 60 UV–Vis spectrophotometer; the scan range for UV–Vis's absorption was between 200 – 800 nm. The crystallographic structure of the films were determined by XRD using a PANalytical X'Pert Pro powder diffractometer with an X'Celerator detector. The system used Fe-filtered Co-Kα radiation (λ = 1.789Å), adjustable divergence, and fixed receiving slits. WITec Raman microscope model alpha300 RAS was used for examining the films' structural organization and Raman spectra. The LWX100 microscope objective was used to focus on an excitation wavelength of 532 nm, using a power of 0.012 W.

3.2.3 Experimental

3.2.3.1 Synthesis of Ag NPS

Ag NPs were synthesized using the chemical reduction method. Specifically, an aqueous solution of $NaBH_4$ (10 mL, 20 mM) was added to a 100 mL aqueous solution containing $AgNO_3$ (0.25 mM) and trisodium citrate (0.25 mM). The reaction mixture was stirred for 30 minutes until a yellow colloidal silver solution formed.

3.2.3.2 PEDOT:PSS samples fabrication

PEDOT:PSS was first filtered through a hydrophilic filter, it was then doped with 1 mL of ethanol ammine before being spin-coated on glass at 3000 rpm for 30 s. Different amounts of Ag NPs were prepared by adding 10, 20, and 30 μL of Ag NPs solution into a 100 ml blend of PEDOT: PSS and ethanol amine. The first solution was without Ag NPs while the other solutions contained varying amounts of Ag NPs. The thin films underwent a 15-minute annealing process at a temperature of 120°C, then followed a cooling process to get them to room temperature.

3.4 Results and Discussion

3.4.1 UV-Vis spectroscopy

The UV/Vis spectrum of the Ag NPs in Figure 3.1a shows an intense peak at 389 nm indicating the formation of Ag NPs. The reduction of Ag^{+} ions to Ag NPs using NaBH4 resulted in the development of a unique absorption spectrum between 350 and 450 nm, attributed to the surface plasmon resonance (SPR) of the metal's conducting electrons in the colloidal silver. The 389 nm intense peak did not expand, indicating that there is little, or no agglomeration as seen in Figure 3.1a [8]. In a study by Zienliska *et al*. similar outcomes were observed. The presence of a significant plasmon band around 400 nm in the silver colloid's spectra confirmed the reduction of Ag^{+} to Ag° in the aqueous phase [12].

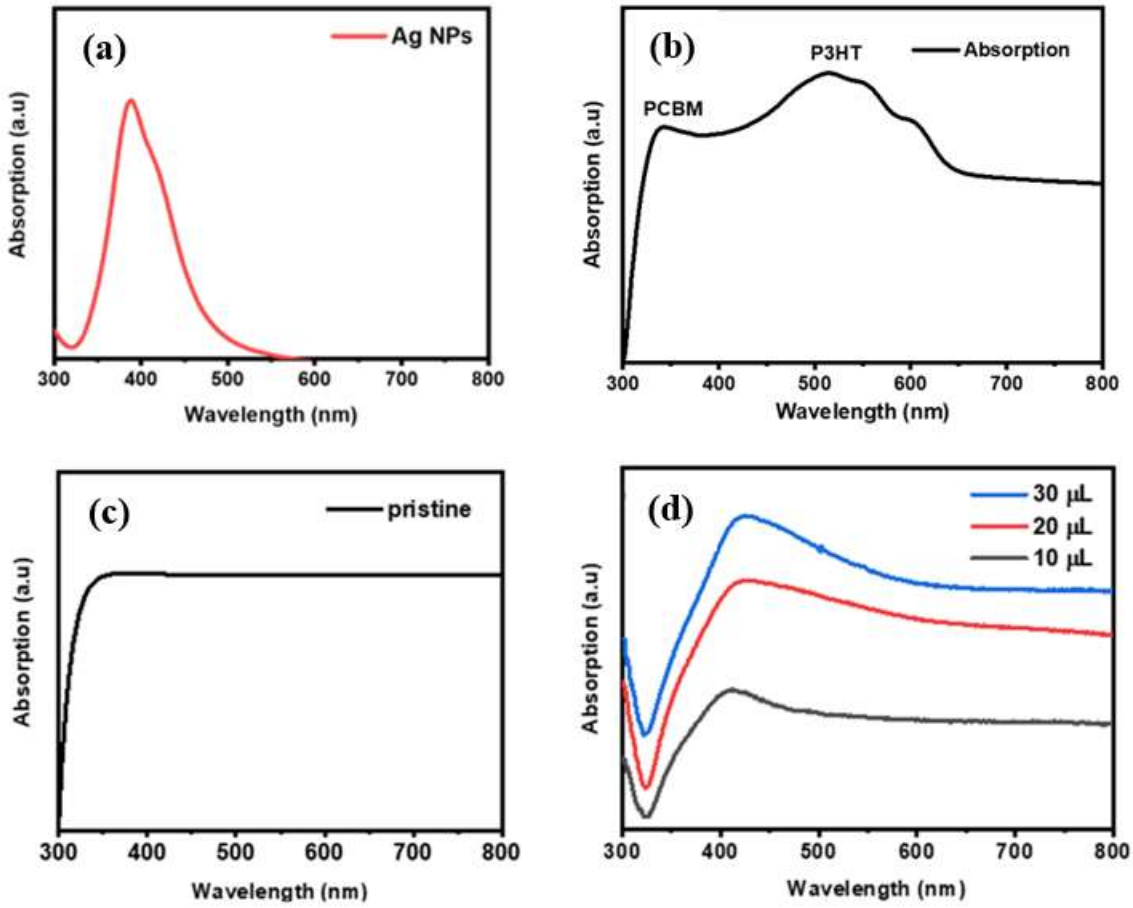

Figure 3.1: UV/ Vis spectra of (a) Ag NPs, (b) P3HT: PCBM, PEDOT: PSS (c) pristine and (d) at different volumes of Ag NPs.

The absorption spectrum of the P3HT: PCBM blend is illustrated in Figure 3.1b There are two primary absorption peaks observed at approximately 340 nm and 510 nm, corresponding to PCBM and P3HT, respectively. P3HT is primarily responsible for the majority of the absorption in the blended film. Its absorbance is higher than that of PCBM, particularly in the 450–600 nm region. At roughly 600 nm, a vibronic structure is observed in regioregular P3HT. We attribute this vibronic structure to the ordered state attained by the regioregular P3HT [13]. Our findings align with those reported in previously published articles [13].

Figure 3.1c and d shows UV-Vis results of PEDOT: PSS at various volumes of Ag NPs. The transparent polymer pristine PEDOT: PSS is shown by the absence of an absorption peak in Figure 3.1c. There is one primary plasmon absorption band at 435 nm in PEDOT: PSS with various volumes of Ag NPs illustrated in Figure 3.1d, which demonstrates that their integration had an impact on the PEDOT: PSS absorption. The peak intensity of 30 µL is higher than the

20 and 10 µL, implying that increasing the volume of Ag NPS results in a proportional increase in the intensity of the maximum plasmon peak. The volume of Ag NPs in the colloidal solution directly correlates with the intensity of an absorption peak [14].

3.4.2 Transmission electron microscopy

Figure 3.2 shows a transmission electron microscopy (TEM) image of water-soluble citrate stabilized Ag NPs and their size distribution. The TEM image (Figure 3.2a) shows that the Ag NPs have elongated spherical morphology and are widely dispersed. The particle size distribution shown in Figure 3.2b indicates that the produced NPs have an average diameter of 22(2) nm, with a size range of 10 – 70 nm. In a chemical synthesis process, the size and distribution of nanoparticles are dependent on the relative speeds of nucleation and growth processes as well as the agglomeration phenomena [15]. Zaheer *et al.*'s findings, as revealed by TEM images, indicated that the silver solution contains well-dispersed spherical NPs with a particle size range of 10 to 30 nm. This is consistent with our research results [16].

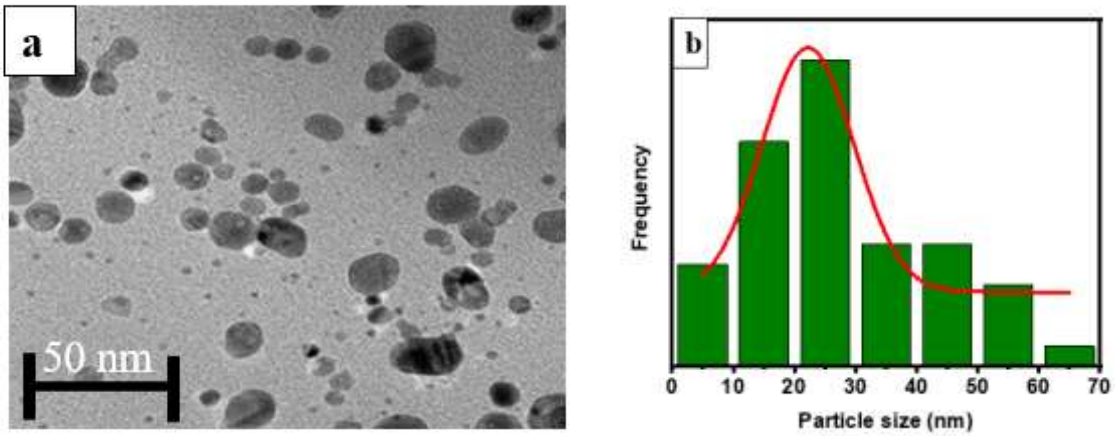

Figure 3.2: (a) TEM image of Ag NPs and (b) graph of particle size distribution curve of Ag NPs.

3.4.3 Scanning electron microscopy

SEM analysis was conducted to examine the surface morphology of PEDOT:PSS at different volumes of Ag NPs. Figure 3.3 shows SEM images of the PEDOT:PSS layer onto the ITO substrate. The images show full coverage of the polymer on top of the ITO; ethanol amine had an impact on this complete coverage since it enabled PEDOT:PSS to attach to the ITO substrate. Various volumes of incorporated Ag NPs in PEDOT:PSS are illustrated as white dots

in Figures 3.3b through d. The visual images in our study are comparable to those of Liu *et al.* [8]. Figure 3.3a is a pristine PEDOT:PSS, the image shows a coarse surface. As shown in Figures 3.3b and c, the Ag NPs were dispersed uniformly across the PEDOT:PSS layer with no clear aggregation, while Ag NPs with the highest volume aggregate into clumps of NPs (Figure 3.3d). Moreover, the NPs exhibit a spherical shape.

It is crucial for the uniform deposition of Ag NPs to prevent any aggregation, as the clustering of Ag NPs may lead to device shortages or undesirable alterations in the emissive properties. These changes can include shifts in the spectrum, alterations in directionality, and even modifications in polarization [17].

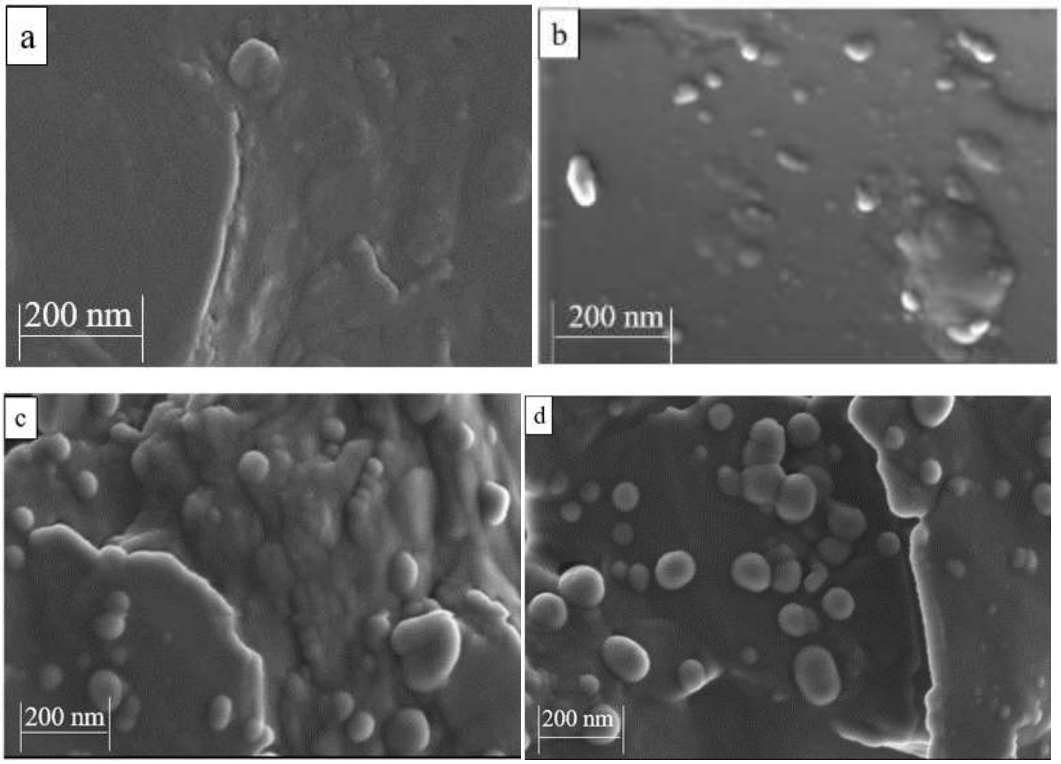

Figure 3.3: SEM images of (a) pristine PEDOT: PSS and the integration of Ag NPs into PEDOT: PSS using (b) 10 µL, (c) 20 µL (d) 30 µL volumes.

3.4.4 Raman spectroscopy

Figure 3.4 shows Raman spectra of PEDOT:PSS at various volumes of Ag NPs. Pristine PEDOT:PSS thin film presents three vital bands at 446, 930, and 1567 cm^{-1} related to (C-S-C),

(O-S), and (C_{∞} -C_{β}) asymmetric stretching, respectively. After the incorporation of Ag NPs, for a volume of 10 µL the spectrum locations change to 436, 925, and 1579 cm^{-1}; however, for 20 µL and 30 µL of Ag NPs, the band positions move to 446, 930, and 1575 cm^{-1} and 441, 925, and 1571 cm^{-1}, respectively. The shifting of these bands results from structural modifications after adding various concentrations of Ag NPs. Which also indicates a blue shift.

According to studies, the band between 1400 and 1500 cm^{-1} is crucial for determining the structure of the PEDOT:PSS chain. Raman spectra's strongest peak at 1435 cm^{-1} is generated by the ($C_{\infty} = C_{\beta}$) symmetric stretching vibration of PEDOT:PSS, indicating the emergence of a shape resembling a quinoid. The findings from Sarkar *et al*. and ours are in good agreement [18]. As a result, it is identified through the analysis of Raman spectra that PEDOT:PSS structure transitions from a benzoid to a quinoid form [19].

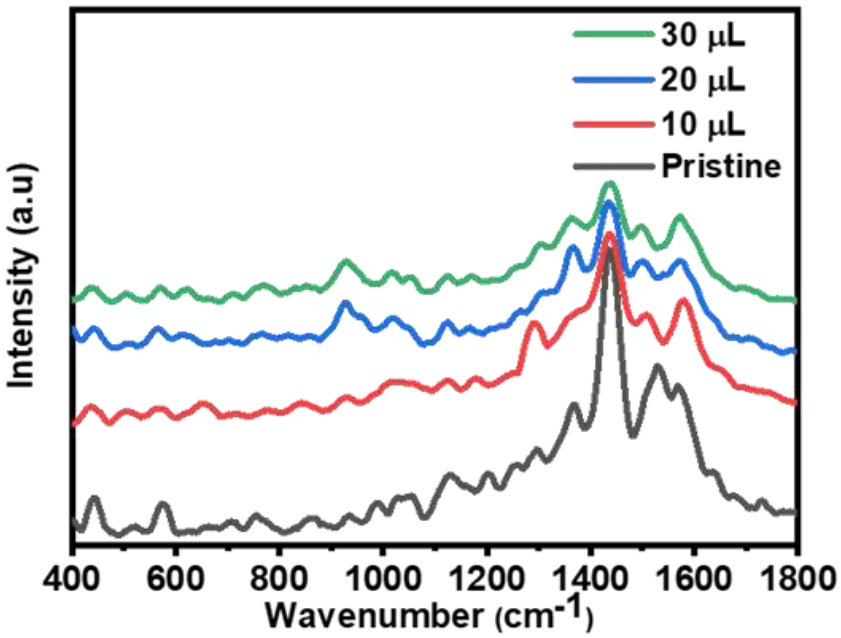

Figure 3.4: Raman spectra of PEDOT: PSS at different volumes of Ag NPs.

3.4.5 XRD diffraction

Figure 3.5 shows XRD patterns of pristine PEDOT:PSS and PEDOT:PSS incorporated with various Ag NPs volumes. In general, PEDOT:PSS exhibits an amorphous nature. According to several research reports [20, 21] a peak associated with PEDOT:PSS that was supposed to exist

at about 25° was absent. Our observations however show a broad diffraction peak at $2\theta \approx 28°$. This implies that there is a very low crystallinity among the polymer chains because of the relatively wider peak [22]. The peaks at 28,17, 27,23, 27,77, and 28,22° are observed for both samples and they are associated with PEDOT:PSS. When nanoparticles are present, PEDOT: PSS films exhibit a composite character, as demonstrated by X-ray diffraction analysis.

After incorporation of the NPs, a sharp diffraction peak emerged at $2\theta \approx 45°$ which corresponds to the (200) crystallographic plane of the face-centred cubic (FCC) phase of Ag [23]. Peak intensity decreases as Ag NPs volume increases due to reduced crystallinity in the film [24].

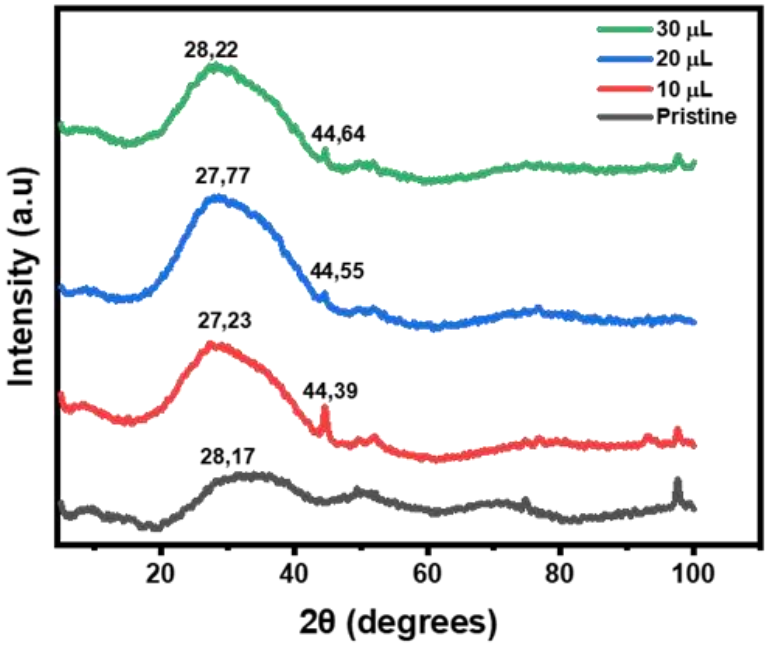

Figure 3.5: XRD patterns of PEDOT:PSS for pristine and at different volumes of Ag NPs

3.5 Conclusion

The Ag NPs were incorporated in the PEDOT:PSS layer to improve light absorption. The TEM analysis indicates that the Ag NPs vary in size from 10 to 70 nm. Based on the TEM images, the NPs are widely scattered and have a primarily spherical morphology. The UV-Vis absorption spectra show that the Ag NPs exhibit a surface plasmon absorption band at a maximum of 389 nm, providing evidence that there are spherical Ag NPs present. The absorption peak in Figure 3.1b demonstrates lower light absorption at 10 µL volume of Ag NPs.

In contrast, the absorption peak at 30 µL volume of Ag NPs exhibits increased light absorption, implying that the incorporation of Ag NPs enhanced PEDOT:PSS absorption.

3.6 References

[1] Kaur, G., et al., *Electrically conductive polymers and composites for biomedical applications.* RSC Advances, 2015. **5**(47): p. 37553-37567.

[2] Ahmad, Z., et al., *Mechanisms for doped PEDOT: PSS electrical conductivity improvement.* Materials Advances, 2021. **2**(22): p. 7118-7138.

[3] Po, R., et al., *Polymer-and carbon-based electrodes for polymer solar cells: Toward low-cost, continuous fabrication over large area.* Solar Energy Materials and Solar Cells, 2012. **100**: p. 97-114.

[4] Duche, D., et al., *Improving light absorption in organic solar cells by plasmonic contribution.* Solar Energy Materials and Solar Cells, 2009. **93**(8): p. 1377-1382.

[5] Xia, Y., K. Sun, and J. Ouyang, *Solution-processed metallic conducting polymer films as transparent electrode of optoelectronic devices.* Advanced materials, 2012. **18**(24): p. 2436-2440.

[6] Barnes, W.L., A. Dereux, and T.W. Ebbesen, *Surface plasmon subwavelength optics.* nature, 2003. **424**(6950): p. 824-830.

[7] Yao, M., et al., *Surface plasmon resonance enhanced polymer solar cells by thermally evaporating Au into buffer layer.* ACS applied materials & interfaces, 2015. **7**(33): p. 18866-18871.

[8] Liu, X.-H., et al., *Plasmonic-enhanced polymer solar cells with high efficiency by addition of silver nanoparticles of different sizes in different layers.* Solar energy, 2014. **110**: p. 627-635.

[9] Lee, J.H., et al., *High efficiency polymer solar cells with wet deposited plasmonic gold nanodots.* Organic Electronics, 2009. **10**(3): p. 416-420.

[10] Shen, H., P. Bienstman, and B. Maes, *Plasmonic absorption enhancement in organic solar cells with thin active layers.* Journal of Applied Physics, 2009. **106**(7).

[11] Pillai, S.a. and M. Green, *Plasmonics for photovoltaic applications.* Solar Energy Materials and Solar Cells, 2010. **94**(9): p. 1481-1486.

[12] Zielińska, A., et al., *Preparation of silver nanoparticles with controlled particle size.* Procedia chemistry, 2009. **1**(2): p. 1560-1566.

[13] Dante, M., J. Peet, and T.-Q. Nguyen, *Nanoscale charge transport and internal structure of bulk heterojunction conjugated polymer/fullerene solar cells by scanning probe microscopy.* The Journal of Physical Chemistry C, 2008. **112**(18): p. 7241-7249.

[14] Medina-Ramirez, I., et al., *Green synthesis and characterization of polymer-stabilized silver nanoparticles.* Colloids and Surfaces B: Biointerfaces, 2009. **73**(2): p. 185-191.

[15] Zheng, N., J. Fan, and G.D. Stucky, *One-step one-phase synthesis of monodisperse noble-metallic nanoparticles and their colloidal crystals.* Journal of the American Chemical Society, 2006. **128**(20): p. 6550-6551.

[16] Khan, Z., et al., *Preparation and characterization of silver nanoparticles by chemical reduction method.* Colloids and Surfaces B: Biointerfaces, 2011. **82**(2): p. 513-517.

[17] Balamurugan, A., K.-C. Ho, and S.-M. Chen, *One-pot synthesis of highly stable silver nanoparticles-conducting polymer nanocomposite and its catalytic application.* Synthetic Metals, 2009. **159**(23-24): p. 2544-2549.

[18] Sarkar, S., et al., *Structural and electrical behaviours of PEDOT: PSS thin films in presence of negatively charged gold and silver nanoparticles: A green synthesis approach.* Synthetic Metals, 2021. **279**: p. 116848.

[19] Sze, P.-W., et al., *The investigation of high quality PEDOT: PSS film by multilayer-processing and acid treatment.* Energies, 2017. **10**(5): p. 716.

[20] White, M.S., et al., *Ultrathin, highly flexible and stretchable PLEDs.* Nature Photonics, 2013. **7**(10): p. 811-816.

[21] Peera, S.G., et al., *Catalytic activity of Pt anchored onto graphite nanofiber-poly (3, 4-ethylenedioxythiophene) composite toward oxygen reduction reaction in polymer electrolyte fuel cells.* Electrochimica Acta, 2013. **108**: p. 95-103.

[22] Tsujimoto, T., T. Takayama, and H. Uyama, *Biodegradable shape memory polymeric material from epoxidized soybean oil and polycaprolactone.* Polymers, 2015. **7**(10): p. 2165-2174.

[23] David, L. and B. Moldovan, *Green synthesis of biogenic silver nanoparticles for efficient catalytic removal of harmful organic dyes.* Nanomaterials, 2020. **10**(2): p. 202.

[24] Lee, H., et al., *Improvement of PEDOT: PSS linearity via controlled addition process.* RSC advances, 2019. **9**(30): p. 17318-17324.

Chapter 4: Fabrication of transparent and flexible Bacterial Cellulose/PVA composite substrate

4.1 Introduction

Cellulose is a natural polymer, produced by plants, and certain bacterial species [1]. It can produce materials that are biocompatible and environmentally friendly [1]. Cellulose fibers can be used to make highly transparent and smooth films which can be used as substrates for solar cells [2, 3]. Bacterial cellulose (BC) is produced by Gram-negative, acetic acid bacteria *Gluconacetobacter xylinus* and it can be found in various sources such as vinegar, fruits, vegetables, and alcoholic beverages [4]. It has been reported that bacteria produce cellulose as a means of protection against ultraviolet radiation, chemical environments, and to facilitate access to oxygen [5, 6].

BC has high crystallinity (60–90%), high mechanical strength, and full biocompatibility [7]. Therefore, due to these unique properties, BC is particularly common and interesting among various sources of cellulose. Additionally, the use of BC eliminates the need for wax, lignin, hemicellulose, and pectic substances all of which are normally found in cellulosic products made from plants [8]. In this study, we report the Fabrication of composite films using BC and Polyvinyl alcohol (PVA) as a binding agent to produce a flexible and transparent substrate.

4.2 Materials and Instrumentation

4.2.1 Chemicals

Sulfuric acid (98%, H_2SO_4), absolute ethanol (C_2H_5OH), ammonium sulfate ($(NH_4)_2SO_4$), sodium hydroxide (NaOH), nitric acid (HNO_3, 55%) sucrose ($C_{12}H_{22}O_{11}$), magnesium sulfate hexahydrate ($MgSO_4.7H_2O$), hydrochloric acid (HCl, 32%), sodium hypochlorite (NaClO), potassium phosphate (KH_2PO_4), dialysis tubing cellulose membrane (flat width 43 mm) and acetone (C_3H_6O) were obtained from Sigma Aldrich. Kombucha tea, green tea (rooibos), brown sugar, and silicon moulds were obtained from South African commercial retailers.

4.2.2 Characterization Techniques

In this investigation, the optical transmittance was measured using an Agilent Cary 60 UV-Vis Spectrophotometer. The UV-Vis transmittance scan range is 200- 400 nm for UV and 400– 800 nm for visible light. Fourier transform infrared (FT-IR) spectra were obtained using a Perkin-

Elmer Spectrum 100 FT-IR Spectrometer (USA) with a diamond crystal ATR accessory within the 4000 – 400 cm^{-1} range. Transmission electron microscope (TEM) images were obtained using a field emission gun transmission electron microscope (FEG-TEM, Jeol 2100). Before TEM imaging, the BC fibers were sonicated and negatively stained with uranyl acetate. Fiber dimensions were calculated using ImageJ Software. Scanning electron microscope (SEM) images were obtained using a field emission scanning electron microscope (FE-SEM Zeiss SEM Microscope Crossbeam-540). SEM images of the BC substrate were obtained at an acceleration voltage of 5.00 kV because of the substrate's sensitivity to the field emission gun. X-ray diffraction analysis (XRD) was carried out using a Bruker, AXS D2 phaser Advance X-ray diffractometer (Germany), using a copper (Cu) source with Kα1 = 0.154 nm. Thermogravimetric analysis of the substrates was measured using a Perkin Elmer Simultaneous Thermal Analyzer (SDT 600) under N2 conditions, heating to a maximum of 850 °C at 10 °C min^{-1}.

4.2.3 Experimental

4.2.3.1 The development of a symbiotic culture of bacteria and yeast (SCOBY)

A 500 ml beaker was sterilized and filled with kombucha tea. Separately, 500 ml of green tea was brewed with boiling water and allowed to cool to room temperature before being mixed with the kombucha tea. Then, 85 grams of commercial brown sugar was added to the kombucha and green tea mixture and stirred until fully dissolved. Two 500 ml beakers, previously sterilized, were equally filled with the mixture. The beakers were kept at room temperature in the dark and covered with semi-permeable fabric. After two weeks, the SCOBY was extracted from the kombucha tea medium for subsequent use in BC biological production.

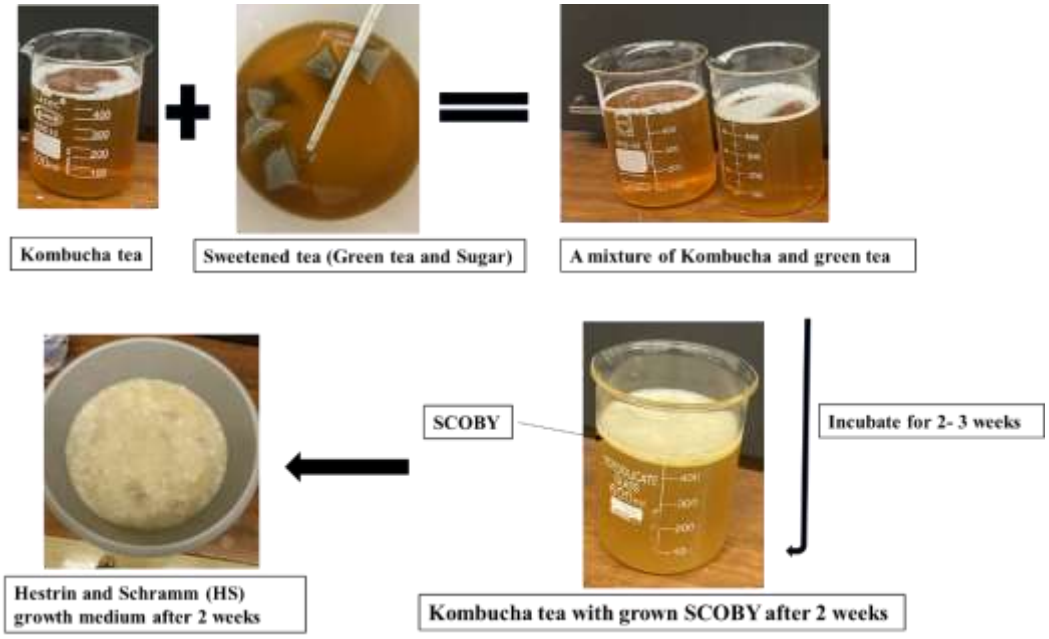

Figure 4.1: A visual representation of the SCOBY growth process.

4.2.3.2 Biological Growth of BC

Following accepted procedures [9], a Hestrin and Schramm (HS) medium was made for the cultivation of BC. A solution of 55 g sucrose, 10 g ammonium sulfate, 10 g yeast extract, 7 g potassium phosphate, and 0.1 g magnesium sulfate heptahydrate was prepared for the HS medium by dissolving all the ingredients in 500 mL of boiling water. The HS medium solution was left to cool to room temperature. The HS medium was transferred to a clean plastic bowl with the SCOBY. A semi-permeable covering was placed over the bowl and was incubated at room temperature in a dark and aerobic area. After two weeks, the BC pellicle was removed and cleaned with water. The BC pellicle was treated with a 0.25 M NaOH solution for 24 hours subsequently, a 15 wt% NaClO solution was used for bleaching. The bleached BC pellicle was rinsed with water and stored in double-distilled water, maintaining a pH of approximately 7.

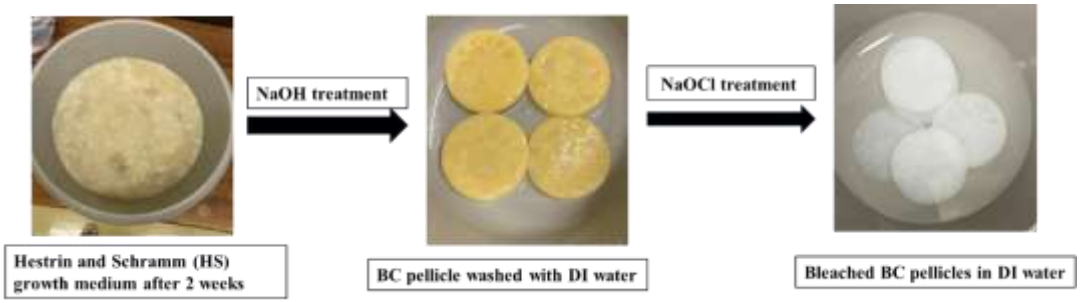

Figure 4.2: A Hestrin and Schramm (HS) medium for the growth of BC using SCOBY.

4.2.3.3 Hydrolysis of BC to BNF

A home blender was used to break down the BC pellicle into smaller pieces and liquefy it. The liquefied BC was vacuum-filtered for an entire night to get rid of extra water, giving it a pulp-like texture. The BC pulp was hydrolysed by stirring it at 55 °C with 60 wt% H_2SO_4, keeping the ratio of 0.5 g BC pulp to 1 mL H_2SO_4. The hydrolysis reaction was stopped after five hours by diluting the reaction fluid tenfold with cold deionized water (DI water). Before starting dialysis, the hydrolysed BC was centrifuged several times to lower the sulfuric acid level. After being added to MCE dialysis tubing, the acid-BC mixture was dialysed in a DI-water reservoir while being constantly stirred. The DI-water's pH was checked regularly by replacing the water every hour until it reached a PH of 6. After being dialysed, the BC mixture was placed in a glass bottle and then examined using SEM and TEM to verify that it was indeed bacterial nanofibers (BNF).

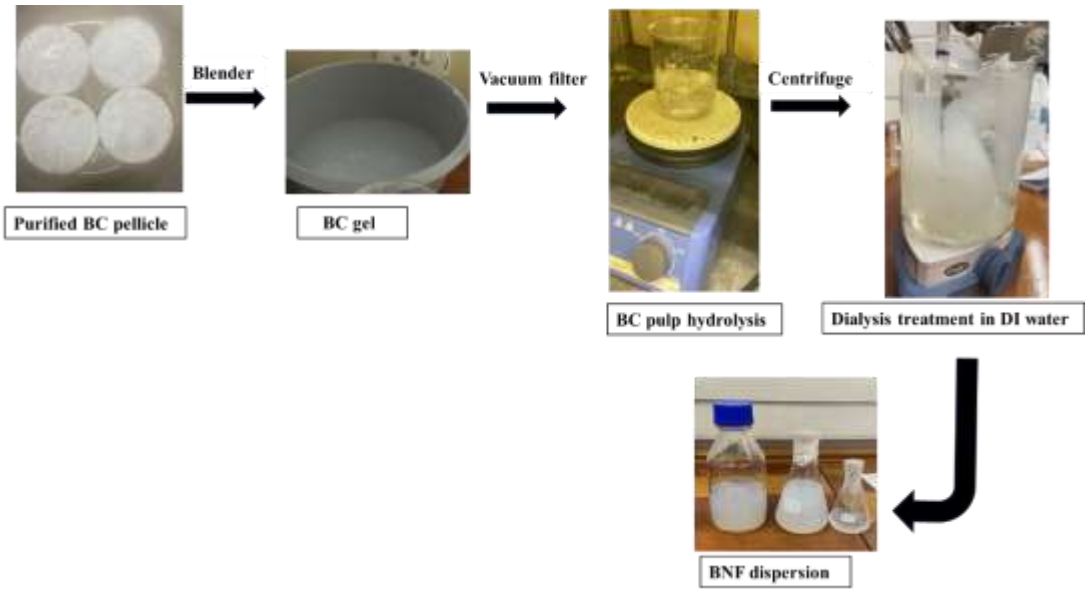

Figure 4.3: The method of hydrolysing bacterial cellulose to produce bacterial nanofibers.

4.2.3.4 Fabrication of BNF: PVA composite substrates

The method employed in this experiment follows that used by Gounden *et al* [10]. Polyvinyl alcohol (PVA) was dissolved in 50 mL of DI water while being continuously stirred under reflux conditions to make a 5 wt% solution. The composition optimization was conducted by varying the BNF-to-polymer ratios to make the substratess. To create a homogenous

combination of BNF and PVA, the required volumes of both solutions were mixed in centrifuge tubes. The tubes were then subjected to ultrasonication for 15 minutes. The homogeneous mixtures were poured into silicon mold and allowed to air-dry for 3 days. PVA was utilized in lesser quantities, due to its role as a strengthening agent and its capacity to enhance the mechanical properties and processing capabilities of BNF substrate.

Table 4.1: The composite substrates's BNF to polymer ratios.

Ratio of BNF: PVA	BNF (10 mg mL $^{-1}$)		PVA (5 wt.%)		Total weight of substrate	
	mL	mg	µL	mg	Expected mg	Actual mg
BNF	5.0	50	0	0	50	49.84 ± 0.06
PVA	0	0	5.0	50	50	49.84 ± 0.06
90:10	4.5	45	100	5	50	49.8± 0.01
70:30	3.5	35	300	15	50	49.97± 0.06
50:50	2.5	25	500	25	50	50.0 ± 0.06

4.3 Results and Discussion

In static growth, bacteria are usually produced in a culture medium that has all the nutrients needed for their growth. During the cultivation process, the culture media is left static, meaning not shaken. As a result, the BC pellicle accumulates at the air-liquid interface, where oxygen is sufficient. A gel-like BC pellicle grown in static conditions is shown in Figure 4.4a. It initially had a natural yellowish colour after the static growth process. The yellow colour is due to the presence of protein and organic impurities obtained from yeast extracts or bacterial cells during the production of BC [11]. Subsequently, the colour turned white after undergoing the purification process (Figure 4.4b). It was treated with sodium hydroxide (NaOH) to remove the organic impurities and consecutively bleached with sodium hypochlorite (NaOCl) which helped with the transparency of the pellicles. The bleaching effect of the NaOCl solution has been reported to be exceptional since it reacts with water to form a weak acid (HOCl) and a strong base (OCl-) [11, 12], as shown by equations (1) and (2).

$$NaOCl + H_2O \rightarrow Na^+ + OCl^- \quad (1)$$

$$OCl^- + H_2O \rightarrow HOCl + OH^- \quad (2)$$

(a) **(b)**

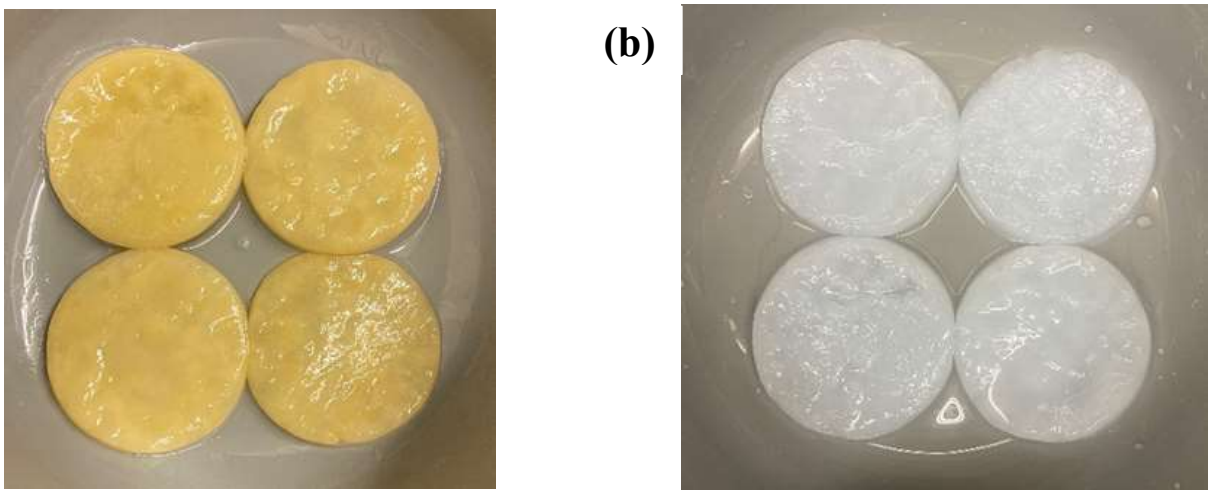

Figure 4.4: BC pellicles produced in static cultivation (a) before and (b) after purification treatment.

The two-step purification process eliminates non-cellulose materials such as proteins and nucleic acids from the pellicle, enabling the development of strong inter- and intra-fibrillar hydrogen bonds [11], also making it possible to see easily inside the gel.

4.3.1 Scanning electron microscopy

Figure 4.5 shows the SEM micrographs of the BC before and after acid hydrolysis. The BC has a porous morphology, with nanofibers arranged in a three-dimensional reticulated network (Figures 4.5a and 4.5b). The fiber morphology closely resembles that described in the study by Abba *et al*. where their fibers measured 200 nm in diameter [13]. The average width of the BC fibers is about 82,17 ± 1,54 nm and the fiber lengths were indeterminable using ImageJ due to their excessive length. Due to its three-dimensional reticulated network, BC is more biocompatible than collagen fiber-woven extracellular matrix [14]. The BC went through hydrolysis to produce bacterial nanofibers (BNF). Sulphuric acid (H_2SO_4) was used to break down the fiber's amorphous region and split down hydrogen bonds of BC fibers resulting in BNF.

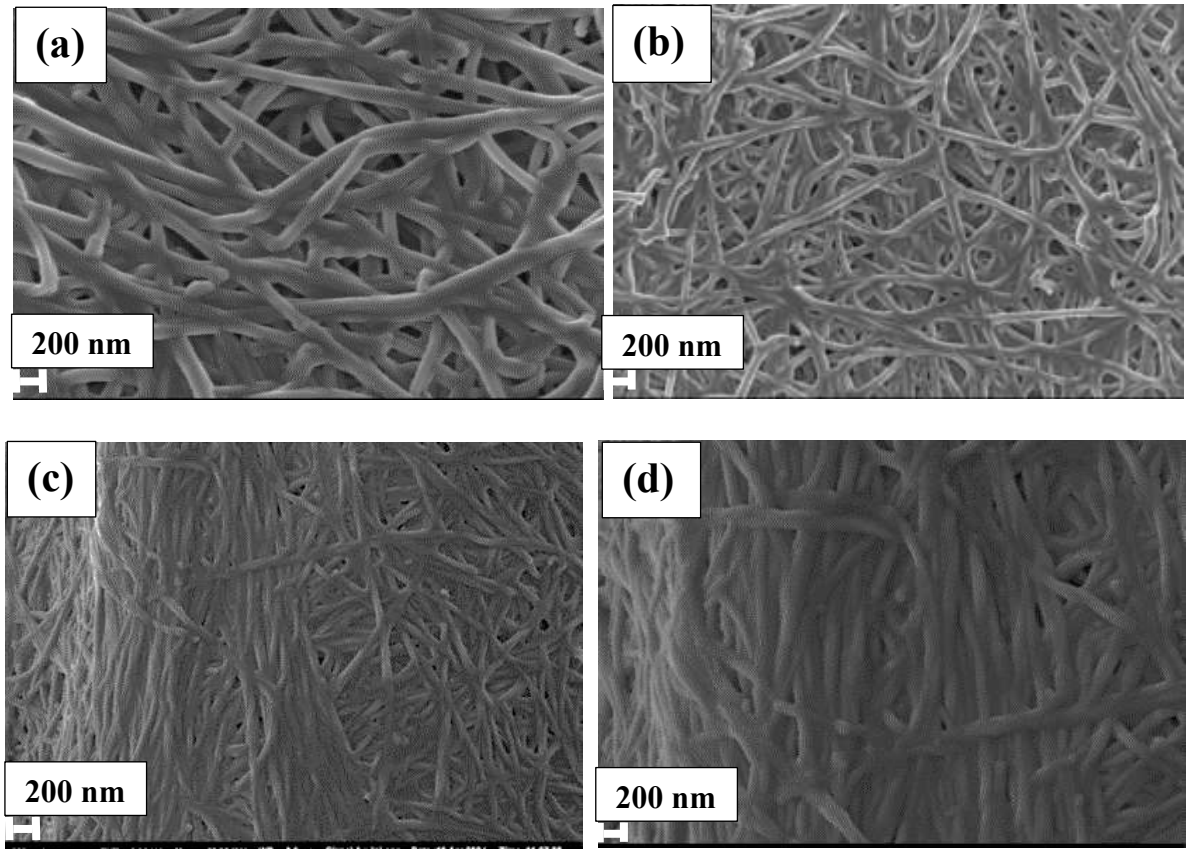

Figure 4.5: SEM images of BC at two different magnifications before hydrolysis (a) 50 KX (b) 100 KX, after hydrolysis (c) 50 KX and (d) 100 KX.

In Figures 4.5c and 4.5d, the fibers of BC after hydrolysis are no longer interconnected with each other. The hydrolysis treatment caused bundles of BNF to aggregate and form. Before hydrolysis, the BC did not contain these bundles (Figures 4.5a and 4.5b). The partial expansion of the nanofibril fragments, whose surfaces tend to stick to one another, appears to be what causes the formation of the BC nanofiber bundles. The crystalline domains of BC are more resistant to hydrolysis than the amorphous regions because they have strong hydrogen bonds, whereas the amorphous regions are poorly aligned and less compact [15].

4.3.2 Transmission electron microscopy

Figure 4.6 shows TEM micrographs of BNF. The morphological and dimensional analyses shown in Figure 4.6a confirmed the hydrolysis of the long BC fibers, resulting in a measurable reduction to the nanometer scale. The needle-like structure of the BNF is similar to that obtained by Dai et al. in their study [16]. The BNF exhibited an average length of 696.16 nm ± 11.55 nm and an average width of 12.18 nm ± 0.61 nm. Comparing the width and length of BC fibers in Figure 4.5a and 4.5b to that of the BNF in Figure 4.6a, it is evident that the hydrolysis reduced both the width and length of the fibers.

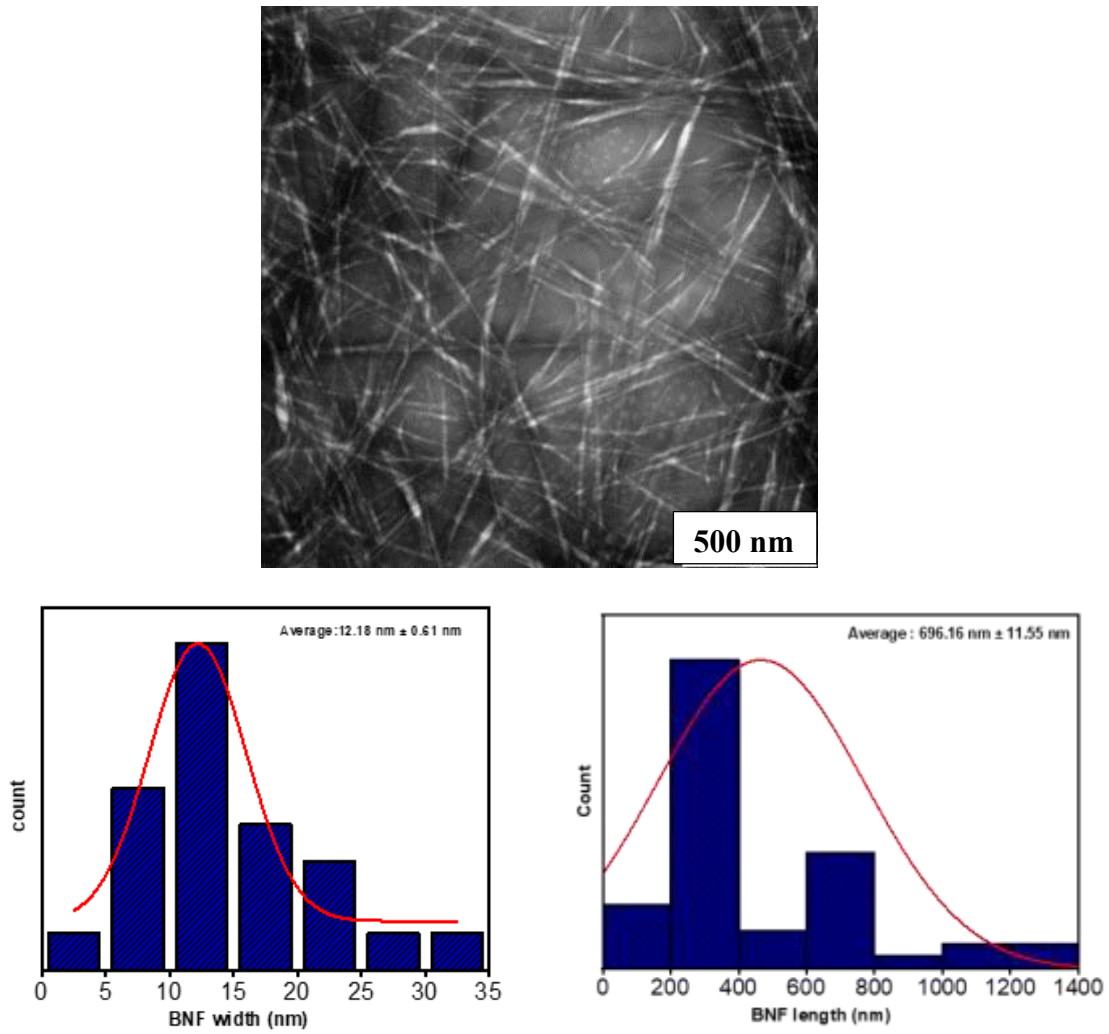

Figure 4.6: TEM image of BNF (a) and size distribution graph of BNF(b) width and (c) length.

4.3.3 XRD diffraction

Cellulose comprises four crystalline allomorphs - celluloses I, II, III, and IV. Cellulose I is the predominant form of cellulose found in nature [16]. Cellulose I's crystalline structure is a combination of two different forms: celluloses Iα (triclinic) and Iβ (monoclinic) [17]. BNF: PVA composite substrates were analyzed using XRD as shown in Figure 4.7b. The diffractograms consistently affirm the semi-crystalline characteristic of BC.

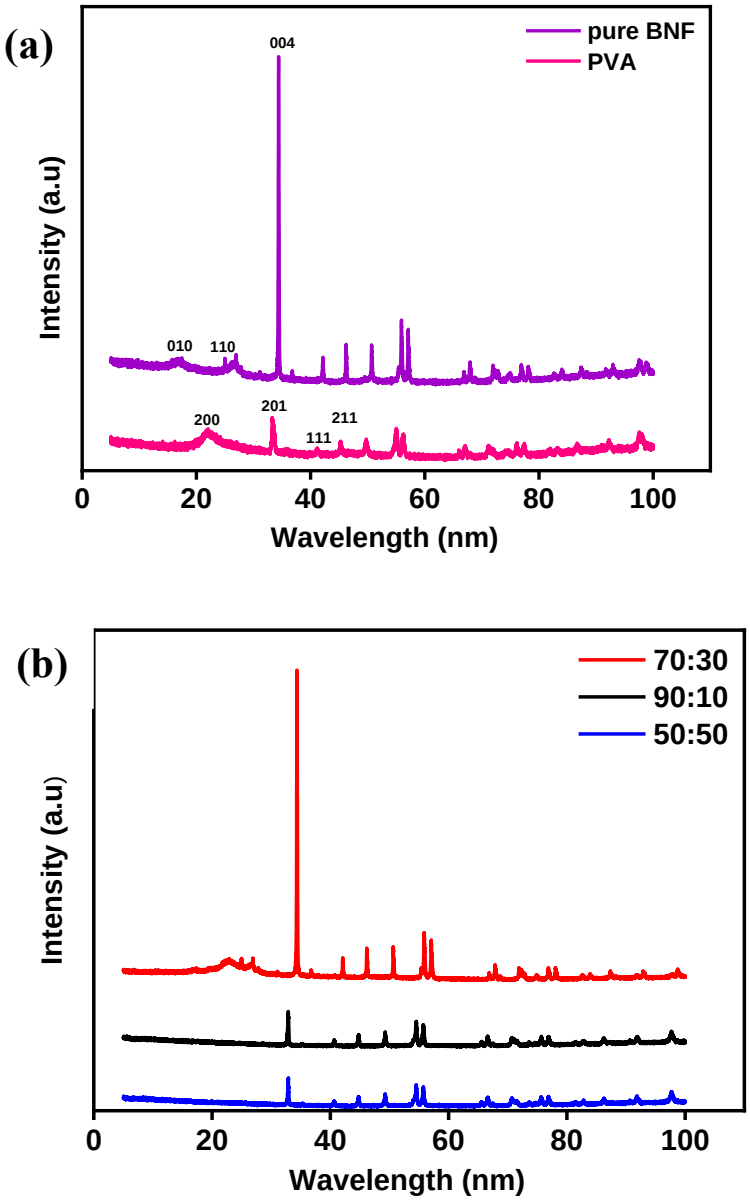

Figure 4.7: XRD diffractograms of (a) Pure BNF and PVA and (b) BNF: PVA composites.

The diffraction patterns of the pure BNF exhibited three distinct peaks that signify the existence of both Iα and Iβ crystal cellulose (Figure 4.7a). The diffraction pattern of the pure BNF sample revealed clear reflections at approximately 16.5°, 22.8°, and 34°, which corresponded to the monoclinic (010), triclinic (110), and (004) crystallographic planes, respectively [16]. However, the BNF/PVA composites display a comparable diffraction pattern profile to that of the pure BNF. This indicates that the semi-crystalline structure remains intact throughout the experimental process. The results of Gouden *et al*. and the results from this study have a strong correlation [10].

4.3.4 FTIR Spectroscopy

Figure 4.8 shows FTIR spectra of pure BNF, PVA, and BNF: PVA composites. The FTIR spectrum peak around 3355 cm^{-1} represents the stretching vibrations of OH groups. The stretching vibrations of cellulose backbone C-H groups are indicated by the peak that is at about 2896 cm^{-1}. BNF's spectrum peaks, which fall between 1500 and 1200 cm^{-1}, are receptive to changes in chemical and molecular structure [18]. The stretching vibrations of C–O–C and C–O are connected to the infrared bands in the 1000 – 1200 cm^{-1} area and are linked to the glycosidic connection of cellulose. These results are comparable to that by Dalei *et al* [19]. Table 4.2 lists the key infrared peaks for the pure BNF, PVA, and composite substrates. Although pure PVA exhibits a spectrum similar to that of the BNF substrate, it lacks vibrations in the 1200 cm^{-1} to 1160 cm^{-1} range, which corresponds to the C-O-C vibrations of BNF.

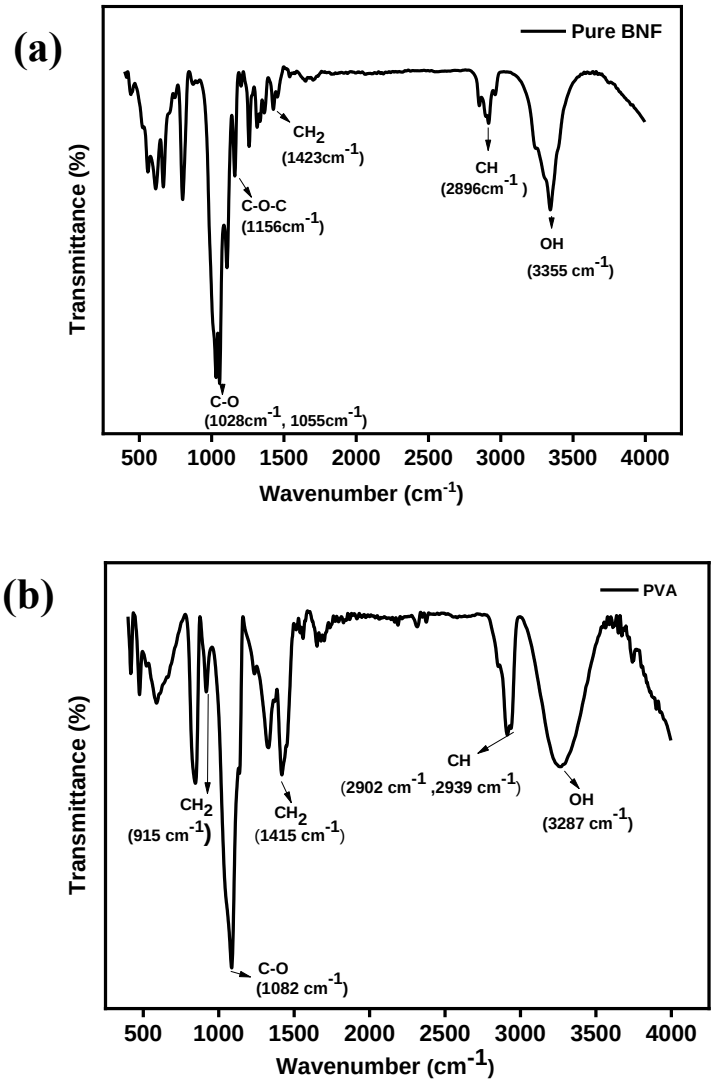

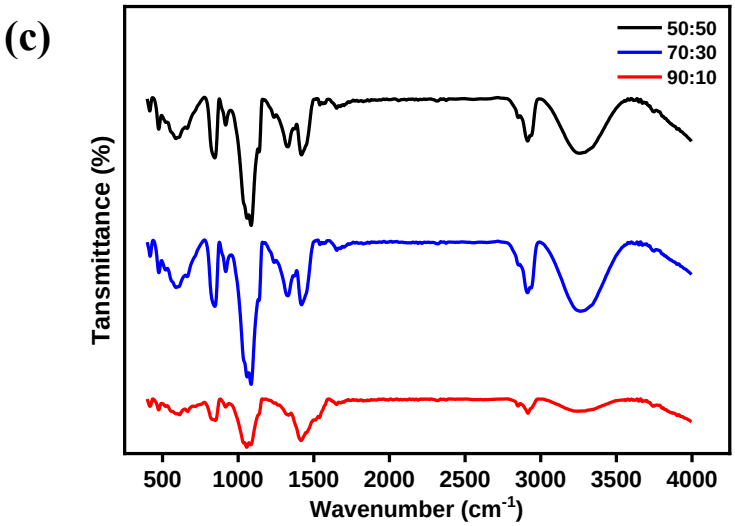

Figure 4.8: FTIR spectroscopy of (a) pure BNF (b) pure PVA (C) BC/PVA composite substrates.

Table 4.2: Key infrared peaks for the pure BNF, PVA, and composite substrates.

Bond assignment	Peak wavenumber (cm^{-1})				
	BNF	PVA	90:10	70:30	50:50
OH (stretch)	3355	3287	-	-	-
CH (stretch)	2896	2902[a], 2939[s]	-	2902[a], 2941[s]	2902[a], 2935
CH_2 (stretch)	1423	1415	1413	1411	1411
C-O (stretch)	1028, 1055	1082	1082	1080	1082
C-O-C (stretch)	1156	-	1143	1141	1143
CH_2 (rocking)	-	915	909	909	911

a – asymmetric, s – symmetric

4.3.5 UV-Vis spectroscopy

A material's transparency signifies the extent to which electromagnetic radiation can pass through it, making it a crucial consideration in the production of transparent electrodes.

Transparent substrates allow light to pass through to the active semiconductor layers of solar cells, where conversion takes place. For this reason, attaining high transparency is essential to optimizing light absorption and, in turn, improving energy conversion efficiency. Figure 4.9 provides a visual representation of the transparent BNF/PVA ratio composite substrates that were fabricated. The composites are made of BNF:PVA ratio as shown in Figure 4.9, the pure BNF substrate was excessively brittle and prone to tearing, making it unsuitable for practical applications. Polyvinyl alcohol (PVA) was selected to enhance the mechanical properties and processing capabilities of BNF substrates while maintaining the original qualities of BNF substrates, such as transparency, and biodegradability. PVA is a versatile synthetic polymer used across various industries due to its emulsifying and adhesive properties, water solubility, and excellent substrate-forming ability. Moreover, PVA has good shrinkage characteristics, is non-toxic and non-carcinogenic, and offers biocompatibility and mechanical strength [20, 21].

Figure 4.9: Visual representation of the produced BNF: PVA ratio composite substrates.

Transparency in the visible region of the electromagnetic spectrum is a crucial requirement for producing transparent substrates. Figure 4.10 shows UV-vis spectra of BNF/PVA composite substrates. The Pure BNF substrate exhibited excellent light transmission of ~ 69% from 750 - 700 nm, then Consistently, sustained ~ 65% transmittance from 690 nm to 500 nm. In comparison to pure BNF substrate, the pure PVA substrate exhibited significantly greater light transmission than the pure BNF substrate. It upheld approximately 80% transmission from 800 nm to 500 nm, with a gradual decline to around 72% between 300 nm and 400 nm. The transparency of the pristine PVA surpassed that of the BNF/PVA composite because the agglomeration of cellulose likely blocked some of the light from getting through. The variance

is attributable to both the purity of the BNF and the structural differences between the substrates.

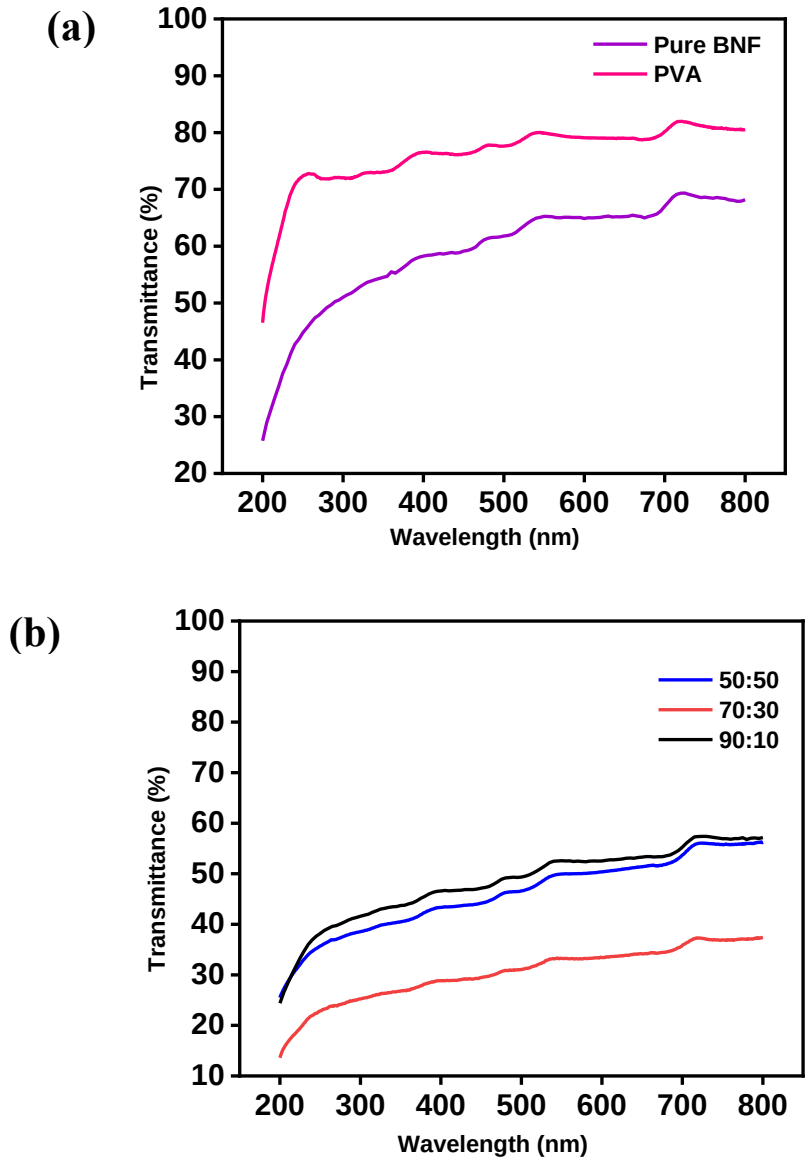

Figure 4.10: Comparison of UV-vis transmittance spectra of (a) Pure BNF and PVA, and (b) BNF/PVA composites.

The 90:10 composite maintained ~ 57% transmittance from 800 nm to 700 nm, which then decreased to around 53% between 690 nm and 500 nm. The 70:30 composite exhibited the lowest transmittance, reaching approximately 37% between 800 nm and 700 nm, which was the lowest among all the composites, and it further decreased to about 34% between 690 nm and 500 nm. As for the 50:50 composite, it showed a 56% transmittance between 800 nm and 700 nm, and it maintained around 51% between 690 nm and 500 nm. There appears to be a more noticeable decline in transmission across all substrates when they enter the ultra-violet

(UV) region of the spectrum, occurring between 400 and 200 nm. By comparing the transmittance of pure BNF and BNF: PVA composites, it is evident that the inclusion of PVA decreased the transmittance of the BNF matrix. This observation reinforces the notion of interaction between BNF and the polymers in the composite substrates. Of all the composite substrates evaluated, the 90:10 ratio appears to be the optimal choice.

4.3.6 Thermogravimetric analysis

Thermogravimetric analysis was used to investigate the thermal performance of pure BNF and PVA substrates. The TGA thermograms of BNF pristine and BNF/PVA composite substrates are shown in Figure 4.11. The first weight loss at lower temperatures between 88 – 200℃ for both BNF pristine and composites is caused by the evaporation of physisorbed and chemically bound water [22]. For pure BNF the second major stage starts at 213 and 381℃ and is caused by the elimination of tiny molecular fragments like hydroxyl and hydroxymethyl groups [23]. The final stage at 382℃, due to the cleavage backbone of PVA composite substrates or the decomposition of carbonaceous matter [22].

As anticipated, the addition of PVA to BNF resulted in composites with lower degradation at temperatures 213- 467℃, as compared to pure BNF, this is due to the structural degradation of PVA composite substrates [24]. This suggests that the addition of PVA changed the thermal properties of BNF, which certainly makes practical sense given that PVA was added to increase BNF's flexibility. The thermograms of PVA were not done due to its rigid nature, the substrate couldn't fit in the thermogravimetric machine bowl. The thermal degradation of PVA/BNF composites at the second stage may have experienced a sharp decrease due to the decreased crystallinity and potentially lower molecular weight of PVA, as these structural parameters can impact the thermal degradation behaviour [25]. These findings are similar to those reported by Ching *et al.* [26].

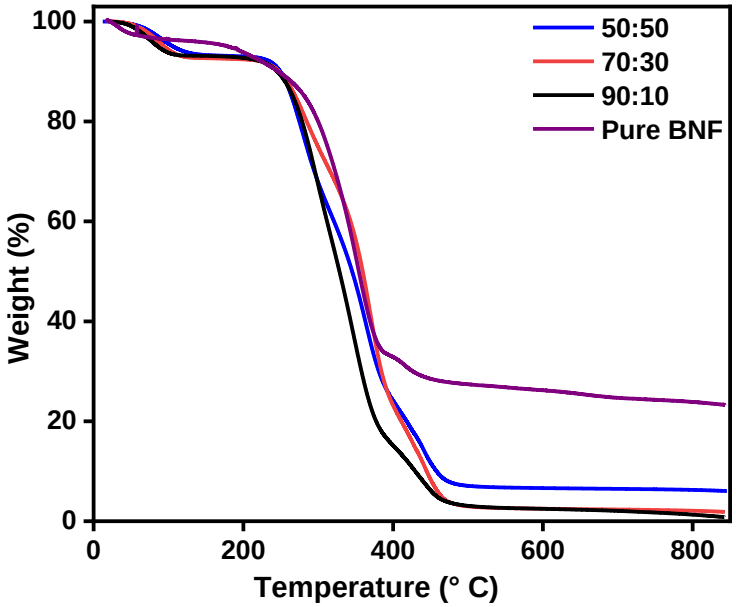

Figure 4.11: Thermogravimetric analysis of pure BNF and BNF/PVA composites.

4.4 Conclusion

This study reports the fabrication of transparent and flexible substrates made from a composite of BNF and PVA polymer used as binding agents. Adding PVA to BNF improved the subtrates's flexibility, although it reduced the natural BNF substrates's optical transmittance. SEM analysis showed that the BC exhibited a porous structure, with nanofibers forming a complex three-dimensional network. Additionally, TEM confirmed that the long BC fibers underwent hydrolysis, leading to a significant reduction in size to the nanometer scale. It was confirmed that the hydrolysis reduced both the width and length of the fibers. The FTIR indicated the stretching vibrations of cellulose backbone C-H groups with a peak at about 2896 cm^{-1} confirming the existence of cellulose. The TGA analysis revealed that the thermal properties of BNF were altered by the addition of PVA. The composites containing PVA showed reduced degradation at temperatures ranging from 213 to 467℃ compared to pure BNF.

4.5 References

[1] Jonas, R. and L.F. Farah, *Production and application of microbial cellulose.* Polymer degradation and stability, 1998. **59**(1-3): p. 101-106.

[2] Zhou, Y., et al., *Recyclable organic solar cells on cellulose nanocrystal substrates. Sci Rep 3: 1536*. 2013.

[3] Chinga-Carrasco, G., D. Tobjörk, and R. Österbacka, *Inkjet-printed silver nanoparticles on nano-engineered cellulose films for electrically conducting structures and organic transistors: concept and challenges.* Journal of Nanoparticle research, 2012. **14**: p. 1-10.

[4] Wang, J., J. Tavakoli, and Y. Tang, *Bacterial cellulose production, properties and applications with different culture methods–A review.* Carbohydrate polymers, 2019. **219**: p. 63-76.

[5] Retegi, A., et al., *Bacterial cellulose films with controlled microstructure–mechanical property relationships.* Cellulose, 2010. **17**: p. 661-669.

[6] Putra, A., et al., *Tubular bacterial cellulose gel with oriented fibrils on the curved surface.* Polymer, 2008. **49**(7): p. 1885-1891.

[7] Klemm, D. and B. Heublein, *h.-P. Fink, A. Bohn.* Angew. Chem. Int. Ed, 2005. **44**: p. 3358-3393.

[8] Shi, Z., et al., *Utilization of bacterial cellulose in food.* Food hydrocolloids, 2014. **35**: p. 539-545.

[9] Hestrin, S. and M. Schramm, *Synthesis of cellulose by Acetobacter xylinum. 2. Preparation of freeze-dried cells capable of polymerizing glucose to cellulose.* Biochemical Journal, 1954. **58**(2): p. 345.

[10] Gounden, D., et al., *Fabrication and processing of bacterial cellulose/silver nanowire composites as transparent, conductive, and flexible films for optoelectronic applications.* Journal of Applied Polymer Science, 2023. **140**(30): p. e54090.

[11] Gea, S., et al., *Investigation into the structural, morphological, mechanical and thermal behaviour of bacterial cellulose after a two-step purification process.* Bioresource technology, 2011. **102**(19): p. 9105-9110.

[12] George, J., et al., *Physico-mechanical properties of chemically treated bacterial (Acetobacter xylinum) cellulose membrane.* World Journal of Microbiology and Biotechnology, 2005. **21**: p. 1323-1327.

[13] Abba, M., et al., *Physicochemical, morphological, and microstructural characterisation of bacterial nanocellulose from Gluconacetobacter xylinus BCZM.* Journal of Natural Fibers, 2022. **19**(11): p. 4368-4379.

[14] Torres, F.G., S. Commeaux, and O.P. Troncoso, *Biocompatibility of bacterial cellulose based biomaterials.* Journal of functional biomaterials, 2012. **3**(4): p. 864-878.

[15] Puri, V.P., *Effect of crystallinity and degree of polymerization of cellulose on enzymatic saccharification.* Biotechnology and bioengineering, 1984. **26**(10): p. 1219-1222.

[16] Watanabe, S., et al., *The conformation of existence of cellulose III1, III2, IV1 and IV2, by the X-ray method.* J. Polym. Lett, 1975. **13**: p. 23-27.

[17] Atalla, R.H. and D.L. Vanderhart, *Native cellulose: a composite of two distinct crystalline forms.* Science, 1984. **223**(4633): p. 283-285.

[18] Atykyan, N., V. Revin, and V. Shutova, *Raman and FT-IR Spectroscopy investigation the cellulose structural differences from bacteria Gluconacetobacter sucrofermentans during the different regimes of cultivation on a molasses media.* AMB Express, 2020. **10**(1): p. 84.

[19] Dalei, G., et al., *Surface modification of cellulose/polyvinyl alcohol biocomposites by non-thermal argon plasma: applications towards biological relevance.* Cellulose, 2019. **26**: p. 2437-2451.

[20] DeMerlis, C. and D. Schoneker, *Review of the oral toxicity of polyvinyl alcohol (PVA).* Food and chemical Toxicology, 2003. **41**(3): p. 319-326.

[21] Muppalaneni, S. and H. Omidian, *Polyvinyl alcohol in medicine and pharmacy: a perspective.* J. Dev. Drugs, 2013. **2**(3): p. 1-5.

[22] Lee, S.-Y., et al., *Nanocellulose reinforced PVA composite films: effects of acid treatment and filler loading.* Fibers and Polymers, 2009. **10**: p. 77-82.

[23] Yang, C. and C. Chen, *Synthesis, characterisation and properties of polyanilines containing transition metal ions.* Synthetic metals, 2005. **153**(1-3): p. 133-136.

[24] Lu, J., T. Wang, and L.T. Drzal, *Preparation and properties of microfibrillated cellulose polyvinyl alcohol composite materials.* Composites Part A: Applied Science and Manufacturing, 2008. **39**(5): p. 738-746.

[25] Um, I.C., et al., *Wet spinning of silk polymer: II. Effect of drawing on the structural characteristics and properties of filament.* International journal of biological macromolecules, 2004. **34**(1-2): p. 107-119.

[26] Ching, Y.C., et al., *Preparation and characterization of polyvinyl alcohol-based composite reinforced with nanocellulose and nanosilica.* BioResources, 2015. **10**(2): p. 3364-3377.

Chapter 5: Electrical conductivity of bacterial cellulose/polyvinyl alcohol composite substrates

5.1 Introduction

Recently, there has been growing interest in developing transparent conductive materials for flexible electrodes [1, 2]. New coating materials are being developed to replace Indium tin oxide (ITO), which isn't ideal for flexible devices. Multiwalled carbon nanotubes (MWCNTs) hold promises for creating flexible, transparent, and electrically conductive films suitable for optoelectronic applications [3]. MWCNTs composed of carbon-carbon bonds have superior mechanical qualities, optical transparency, and high electrical conductivity making them ideal for use as an electronic material [4-6]. Their ability to significantly boost the electrical conductivity of the bacterial cellulose (BC) composite with even a tiny input makes this carbon-based material exceptional, adding MWCNTs to a BC matrix can make it electrically conductive [7].

Composites made of a network of one-dimensional conducting wires exhibit much higher optical transparency and conductivity than those covered with conducting spheres [8]. Therefore, in this study, aqueous MWCNT dispersion containing a surfactant was dispersed in a BC polymer matrix to prepare a conductive transparent, and flexible composite. To stabilize the MWCNTs against van der Waals attraction and reduce the harm that chemical alteration could do to the intrinsic qualities of each nanotube, they were sonicated in cationic cetyltrimethylammonium bromide (CTAB) aqueous solution [9, 10]. Since water is not a good solvent for MWCNTs, a surfactant was utilized to distribute the MWCNTs in water. MWCNTs were uniformly adsorbed and embedded in BNF/PVA. Investigations were also conducted on the morphology and electrical conductivity of the BNF/PVA/MWCNTs composite substrate.

5.2 Materials and Instrumentation

5.2.1 Chemicals

Cetyltrimethylammonium bromide ($C_{19}H_{42}BrN$) and multiwall carbon nanotube (MWCNT) were received in its pure form (98%) were purchased from Sigma Aldrich South Africa, and BNF/PVA substrates were fabricated as part of the experimental process in Chapter 4.

5.2.2 Characterisation Techniques

The transparency of the substrates was measured across wavelengths ranging from 200 to 800 nm using an Agilent 60 UV-visible spectrophotometer (Agilent Technologies, Germany). The electrical conductivity of the MWCNT-adsorbed BNF/PVA substrates was measured using the Ossila four-probe technique. The morphology of electrically conductive transparent BNF/PVA substrate was observed using a field emission scanning electron microscope (FE-SEM Zeiss SEM Microscope Crossbeam-540) and field emission gun transmission electron microscope (FEG-TEM, Jeol 2100).

5.2.3 Experimental

5.2.3.1 Incorporation of multiwalled carbon nanotubes in bacterial cellulose matrix

The method employed in this experiment follows that used by Yoon et al. [7]. Different concentrations of MWCNTs were dispersed in DI water with a cationic CTAB surfactant. The concentrations used were 0.01 wt%, 0.03 wt%, and 0.05 wt% of MWCNTs, along with 0.1 wt%, 0.2 wt%, and 0.3 wt% of CTAB surfactant respectively. The MWCNTs/CTAB solution was sonicated using a sonicator with a nominal frequency of 28 kHz and a power of 600 W for 7 h at 25 °C. Once a homogeneous aqueous dispersion of MWCNTs/CTAB had been obtained. The BNF/PVA composite substrates were then immersed into different concentrations of MWCNTs/CTAB by ultrasonic for 12 h at room temperature. The MWCNTs adsorbed BNF/PVA composite substrates obtained after sonication were further washed with DI water to remove MWCNTs/CTAB, that was not absorbed on BNF/PVA substrate and vacuum dried for water removal.

5.3 Results and Discussion

5.3.1 Morphological properties of Multiwalled Carbon nanotubes

The SEM image in Figure 5.1a shows a cylindrical morphology of the pure MWCNTs that is identifiable by their coiled tube bundle shape [11]. EDX was used to identify the chemical compositions detected in the pure MWCNT as shown in Figure 5.1b. The EDX findings show

that the composition of the MWCNTs is predominantly carbon and there are no inorganic or metal contaminants present in the pure MWCNTs which confirms the purity of the material.

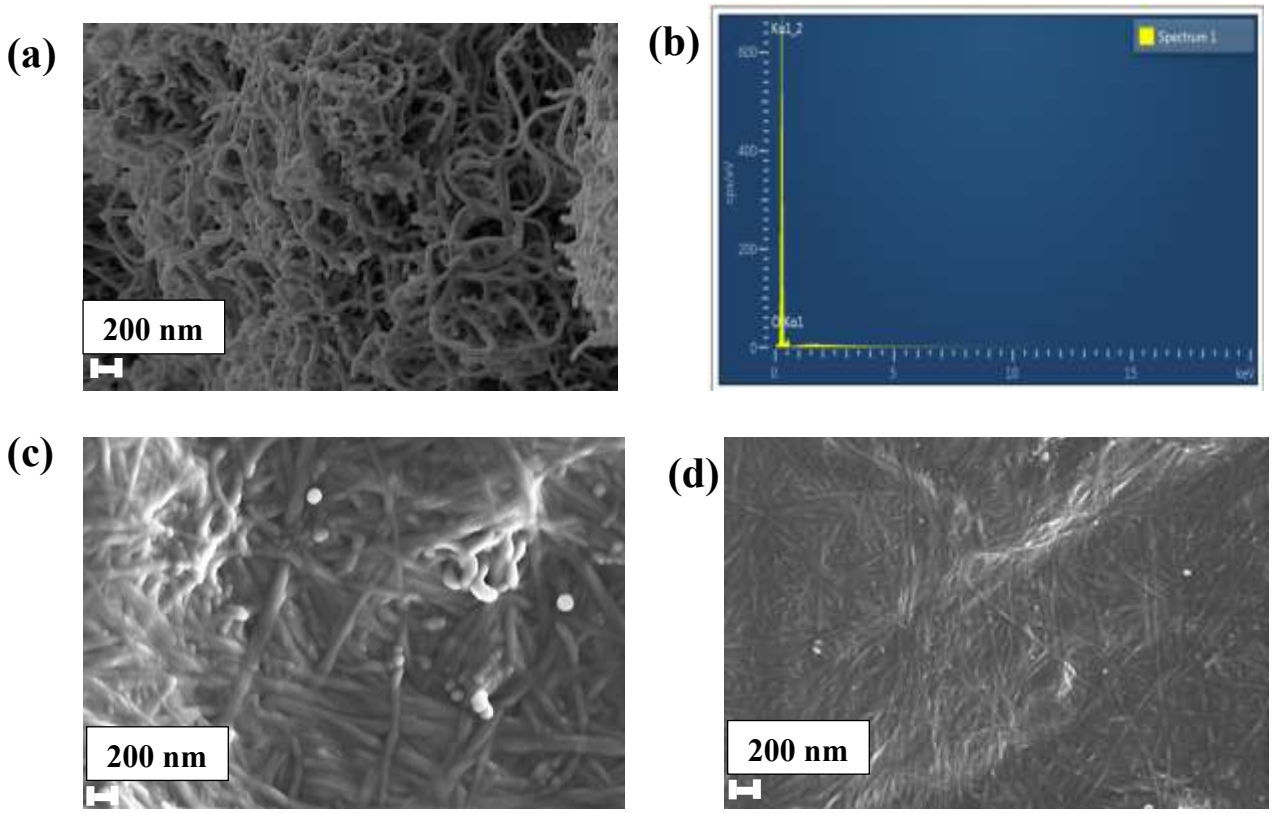

Figure 5.1: (a) SEM image of pure MWCNT, (b) EDX patterns of MWCNT, SEM images of BNF/PVA/MWCNTs at different magnifications (c) 100KX and (d) 50KX.

Figure 5.1c and d shows SEM images of BC/MWCNTs at different magnifications. The adhesion of the MWCNTs on the surface of the BNF/PVA substrate is because of the interaction between the cellulose and the oxygen-containing species on the nanotubes, such as carboxylic acid groups introduced during the purification process [9, 10]. One of the most crucial requirements for achieving uniform conductivity throughout a composite is the homogeneous dispersion of MWCNTs in a polymer matrix. Two distinct domains were identifiable from Figures 5.1c and d; a continuous network of BNF microfibrils and incorporated MWCNTs distributed throughout. Due to their high conductivity, the bright areas in the images are identified as MWCNTs [12]. These MWCNTs were uniformly dispersed throughout the BNF matrix without aggregating as shown in Figures 5.1c and d. The uniformly dispersed MWCNTs enhanced the conductivity of the BNF matrix due to the formation of conductive networks throughout the insulating matrix [12].

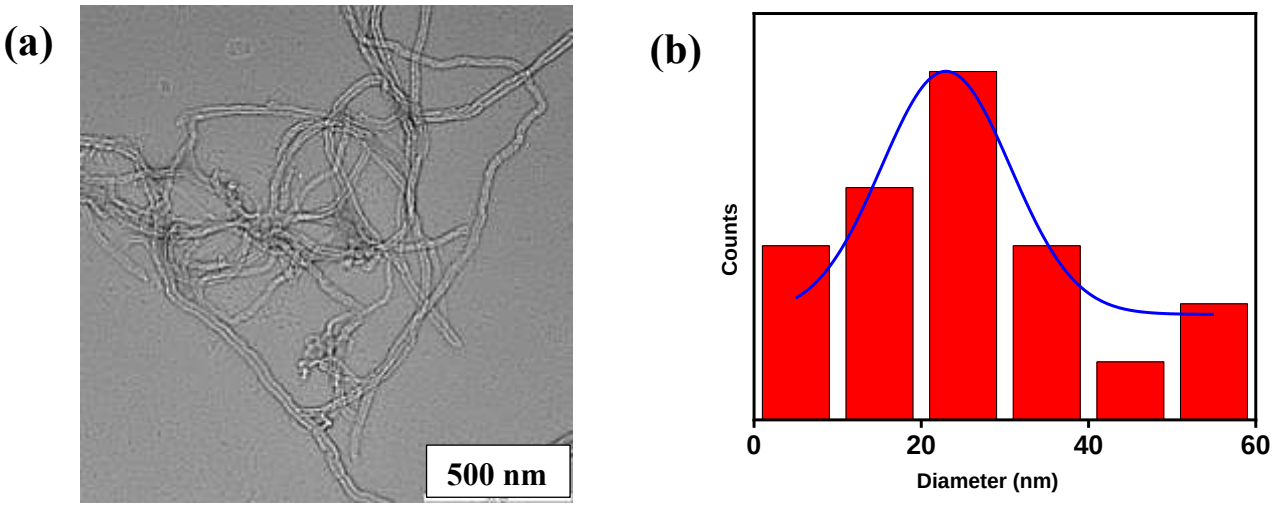

Figure 5.2: (a) TEM microscopy of MWCNTs and (b) size distribution graph.

The TEM image in Figure 5.2a shows that the nanotubes identified are homogeneous, with sizes roughly ranging from 22.94 ± 2,11 nm. The image shows that the MWCNTs are bundles with unique long tubular structures. The tubes exhibit smooth surfaces with no visible defects. The images are consistent with other studies that presented TEM images of MWCNTS showing similar findings [13, 14].

5.3.3 UV-vis spectroscopy

The presence of MWCNTs enhances the substrate's conductivity; however, a higher concentration of MWCNTs within the substrate results in decreased transparency. The optical transmittance of BNF/MWCNTs composites is demonstrated in Figure 5.3. The transparency of BNF/PVA substrates can be affected by scattering, absorption, and reflection. The medium doesn't scatter if the scattering centers are less than 10 nm of the wavelength. Since BNF fibers have cross sections that are roughly 10 nm in diameter, they can be used as reinforcement networks in transparent substrates. Even high fiber content composites show some scattering, though [15]. The concentration of the aqueous MWCNT dispersion had an expected effect on the transmittance of the transparent electrically conductive substrates.

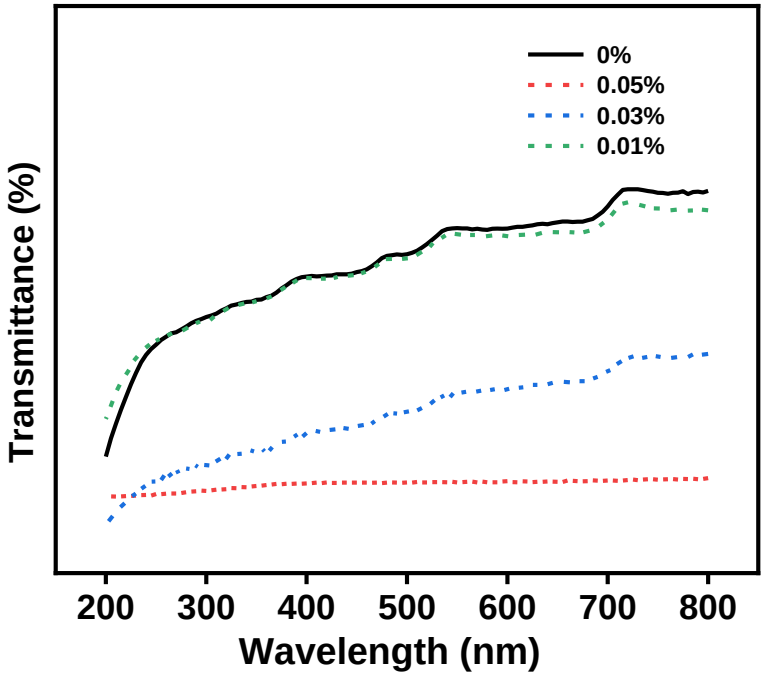

Figure 5.3: Optical transparency of MWCNT-adsorbed substrates at varying MWCNT.

The 0.01% composite substrates exhibited low transmittance within the visible light wavelength range of 400–800 nm, ranging from 50% to 53%. The 0.03% substrates showed even lower light transmittance than the 0.01% composite substrates, with values decreasing from 37% to 27% between 800 nm and 400 nm. The spectra for the 0.05% sustrates remained relatively stable between 800 nm and 350 nm with a transparency of 22%. The transmittance spectra indicate that using a higher concentration of MWCNT dispersion during fabrication resulted in electrically conductive transparent substrates with reduced transparency. Given the same reaction time and a higher concentration of MWCNT dispersion, it is fair to expect that more MWCNTs might adsorb on the BNF substrate.

5.3.4 Electrical conductivity

Bacterial cellulose is naturally non-conductive but can be made conductive by adding conductive nanomaterials. In general, electrical conductivity is influenced by both the incorporated materials and the polymer matrix [16, 17]. In these composite substrates, the polymer layer within the connections between nanotubes serves as a highly resistive segment along the electrical pathway. This impedes efficient carrier transport between the MWCNTs and accounts for the fluctuation-induced tunnelling observed in conductivity models [18]. As shown in Figure 5.4, the substrates were made conductive by incorporating MWCNTs. According to these results, there's a network structure that develops between the MWCNTs in

the polymer matrix, which facilitates electron transport by electron hopping along the MWCNTs interconnections or tunnelling across the BNF [16].

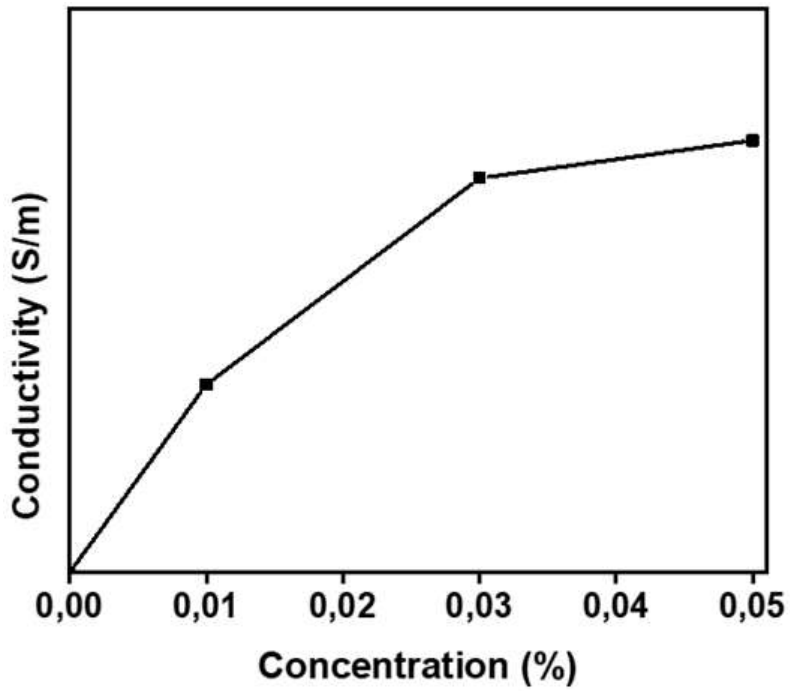

Figure 5.4: Graphical representation of the conductivity of MWCNT-adsorbed substrates at varying MWCNT concentrations.

When the electrically conductive transparent substrates were made from 0.01, 0.03, and 0.05 % MWCNT dispersions, respectively, their corresponding electrical conductivities were 1.0×10^{-2}, 2.1×10^{-2}, and 2.3×10^{-2} S/cm. The results in Figure 5.4 show that the conductivity measured for the BNF/ MWCNTs substrates increases as the MWCNTs concentration increases. The 0.01% showed a lower conductivity among all the other substratess. This was expected as reduced amounts of dispersed MWCNTs on the surface of the substrate hinder current flow as there will be a decrease in contact of the MWCNTs across the surface of the BNF/PVA substrates, thereby inducing lower conductivity values [19]. These results align with those of other studies conducted in the past [7].

5.4 Conclusion

This study reports on the fabrication of conductive, transparent, and flexible substrates as a composite of BNF, PVA as a reinforcing agent, and MWCNTs as the conductive material. The SEM and TEM images revealed that the MWCNTs formed bundles with distinctive long tubular structures. The EDX analysis confirmed the absence of any contaminants. The transmittance spectra showed that increasing the concentration of MWCNT dispersion led to electrically conductive transparent substrates with decreased transparency. The electrical conductivity measured for the BNF/MWCNTs substrates increases as the MWCNT concentration increases. It was evident that the conductivity of the substrates was impacted by the increase in MWCNT concentration.

5.5 References

[1] Saran, N., et al., *Fabrication and characterization of thin films of single-walled carbon nanotube bundles on flexible plastic substrates.* Journal of the American Chemical Society, 2004. **126**(14): p. 4462-4463.

[2] Lewis, J., et al., *Highly flexible transparent electrodes for organic light-emitting diode-based displays.* Applied Physics Letters, 2004. **85**(16): p. 3450-3452.

[3] Zhang, D., et al., *Transparent, conductive, and flexible carbon nanotube films and their application in organic light-emitting diodes.* Nano letters, 2006. **6**(9): p. 1880-1886.

[4] Coleman, J.N., U. Khan, and Y.K. Gun'ko, *Mechanical reinforcement of polymers using carbon nanotubes.* Advanced materials, 2006. **18**(6): p. 689-706.

[5] Cao, Q., et al., *Highly bendable, transparent thin-film transistors that use carbon-nanotube-based conductors and semiconductors with elastomeric dielectrics.* Advanced Materials, 2006. **18**(3): p. 304-309.

[6] Gruner, G., *Carbon nanotube films for transparent and plastic electronics.* Journal of Materials Chemistry, 2006. **16**(35): p. 3533-3539.

[7] Yoon, S.H., et al., *Electrically conductive polymeric membranes by incorporation of carbon nanotubes.* Molecular Crystals and Liquid Crystals, 2007. **464**(1): p. 103/[685]-108/[690].

[8] Poddar, M.K. and P.K. Dikshit, *Recent development in bacterial cellulose production and synthesis of cellulose based conductive polymer nanocomposites.* Nano Select, 2021. **2**(9): p. 1605-1628.

[9] Wang, H., et al., *Dispersing single-walled carbon nanotubes with surfactants: a small angle neutron scattering study.* Nano Letters, 2004. **4**(9): p. 1789-1793.

[10] Kim, H.S., et al., *Carbon Nanotube-Adsorbed Electrospun Nanofibrous Membranes of Nylon 6.* Macromolecular rapid communications, 2006. **27**(2): p. 146-151.

[11] Sheng, G., et al., *Kinetics and thermodynamics of adsorption of ionizable aromatic compounds from aqueous solutions by as-prepared and oxidized multiwalled carbon nanotubes.* Journal of hazardous materials, 2010. **178**(1-3): p. 505-516.

[12] Gao, J., et al., *Continuous spinning of a single-walled carbon nanotube− nylon composite fiber.* Journal of the American Chemical Society, 2005. **127**(11): p. 3847-3854.

[13] Dooher, T. and D. Dixon, *Multiwalled carbon nanotube/polysulfone composites: Using the Hildebrand solubility parameter to predict dispersion.* Polymer composites, 2011. **32**(11): p. 1895-1903.

[14] Al-Hobaib, A.S., et al., *Modification of thin-film polyamide membrane with multi-walled carbon nanotubes by interfacial polymerization.* Applied Water Science, 2017. **7**: p. 4341-4350.

[15] Yano, H., et al., *Optically transparent composites reinforced with networks of bacterial nanofibers.* Advanced Materials, 2005. **17**(2): p. 153-153.

[16] Koizhaiganova, R.B., et al., *Double-walled carbon nanotube (DWCNT)–poly (3-octylthiophene)(P3OT) composites: Electrical, optical and structural investigations.* Synthetic metals, 2009. **159**(23-24): p. 2437-2442.

[17] López-Mata, C., et al., *Optical and morphological properties of chemically synthesized poly3-octylthiophene thin films.* Thin Solid Films, 2005. **490**(2): p. 189-195.

[18] Abu-Abdeen, M., A.S. Ayesh, and A.A. Al Jaafari, *Physical characterizations of semi-conducting conjugated polymer-CNTs nanocomposites.* Journal of Polymer Research, 2012. **19**: p. 1-9.

[19] Gounden, D., et al., *Fabrication and processing of bacterial cellulose/silver nanowire composites as transparent, conductive, and flexible films for optoelectronic applications.* Journal of Applied Polymer Science, 2023. **140**(30): p. e54090.

Chapter 6

6.1 Conclusion and Future Work

Herein we focused on improving and developing materials to enhance the layers of OSCs, thereby boosting their overall performance. Specifically, the study aimed to improve the absorption of PEDOT:PSS (Chapter 3) and to develop a flexible, transparent, and conductive electrode that can serve as a substrate in OSCs (Chapters 4 and 5).

In Chapter 3 the objective was to enhance light absorption in PEDOT:PSS using plasmonic nanoparticles. Ag NPs were employed to increase the absorption of PEDOT:PSS. Initially, chemical reduction was utilized to synthesize the plasmonic NPs. Subsequently, the NP solution was mixed with PEDOT:PSS and spin-coated onto substrates.

The SEM analysis confirmed the successful incorporation of Ag NPS in the PEDOT:PSS layer. Dispersed spherical Ag NPs with sizes 10 to 70 nm could be seen in the PEDOT:PSS layer. The XRD spectra of PEDOT:PSS/Ag exhibited a sharp diffraction peak that emerged at $2\theta \approx 45°$ which corresponds to the (200) crystallographic plane revealing the face-centered cubic (FCC) phase of Ag. The UV-Vis absorption spectra of Ag NPs exhibited a surface plasmon absorption band at a maximum of 389 nm, indicating spherical Ag NPs' existence. The UV-vis absorption spectra of pristine PEDOT:PSS did not show any absorption peak because PEDOT: PSS does not absorb. However, the primary plasmon absorption band at 435 nm proved that the integration of Ag NPS had an impact on PEDOT:PSS absorption.

In Chapter 4 the objective was to fabricate a transparent and flexible film using BC. The BC was grown in static cultivation and converted to BNF using hydrolysis then combined with PVA to enhance the mechanical strength of the film. SEM showed a porous morphology, with nanofibers arranged in a three-dimensional reticulated network. The FTIR spectroscopy revealed asymmetric stretching vibrations of C-O-C associated with an absorption band observed at around 1160 $cm^{-3,}$ demonstrating cellulose's genuine presence and purity. When comparing the transmittance of pure BNF and BNF: PVA composites, it was evident that the inclusion of PVA decreased the transmittance of the BNF matrix. The XRD showed that the diffraction patterns of the pure BNF exhibited three distinct peaks that signified the existence of both Iα and Iβ crystal cellulose.

In Chapter 5 the objective was to make BNF/PVA composite film conductive using multiwalled carbon nanotubes through the immersion method, The EDX findings showed that the composition of the MWCNTs is predominantly carbon, with no inorganic or metal contaminants present in the pure MWCNTs which confirmed the purity of the material. While the MWCNTs contributed to the film's conductivity, the number of MWCNTs inside the film reduced transparency. The concentration of the aqueous MWCNT dispersion had an expected effect on the transmittance of the transparent electrically conductive film. The electrical conductivity measured for the BC/ MWCNTs film increases as the MWCNT concentration increases.

6.2 Future work

Future studies may explore the integration of this substrate into organic solar cells to investigate the compatibility of the BNF/PVA/MWCNT substrate with organic solar cells and assess any improvements in overall device performance. Additional research could explore the integration of conductive nanoparticles to enhance the charge transfer and electrical conductivity of the composite. This could involve exploring the use of materials like graphene or metal oxides that may improve conductivity without drastically decreasing the transparency of the substrate.